Microgravity Application Program / Biotechnology

Mid Term Report for ESA-Project
ESTEC Contract # 14592/00/NL/SH
MAP AO-99-030 / AO-2004-125,
CCN 001, CCN 002, CCN 003

Phases I, II "2D and 3D Quantification of Bone Structure and its Changes in Microgravity Condition by Measures of Complexity"

Phase III "Assessing the Influence of Microarchitecture on the Mechanical Performance of Bone and its Changes in Microgravity from in-vivo Measurements"

Coordinator:

Peter Saparin (PS)	Max Planck Institute (MPI) of Colloids and Interfaces, Germany (MPICI)

Team Members:

Peter Fratzl (PF)	MPI of Colloids and Interfaces, Germany (MPICI)
Richard Weinkamer (RW)	MPI of Colloids and Interfaces, Germany (MPICI)
John Dunlop (JD)	MPI of Colloids and Interfaces, Germany (MPICI)
Davide Ruffoni (DR)	MPI of Colloids and Interfaces, Germany (MPICI)
Dieter Felsenberg, (DF)	Campus Benjamin Franklin, Charité, Germany (CBF)
Gisela Beller (GB)	Campus Benjamin Franklin, Charité, Germany (CBF)
Jürgen Kurths (JK)	University Potsdam, Germany (UoP)
Norbert Marwan (NM)	University Potsdam, Germany (UoP)
Hans-Christian Hege (CH)	Zuse Institute, Berlin, Germany (ZIB)
Steffen Prohaska (SP)	Zuse Institute, Berlin, Germany (ZIB)
Klaus Klaushofer (KK)	Ludwig Boltzmann Institute of Osteology, Austria (LBIO)
Paul Roschger (PR)	Ludwig Boltzmann Institute of Osteology, Austria (LBIO)
Jörg Haller (JH)	Ludwig Boltzmann Institute of Osteology, Austria (LBIO)
Nadja Fratzl-Zelman (NFZ)	Ludwig Boltzmann Institute of Osteology, Austria (LBIO)
Zandieh Shahin (ZS)	Ludwig Boltzmann Institute of Osteology, Austria (LBIO)
Alexey Tatarinov (AT)	Riga Technical University, Latvia (RTU, sub-contract)
Bruno Koller (BK)	Scanco Medical AG, Switzerland (Scanco, Industry)
Christian Asbeck (CA)	Siemens AG, Forchheim, Germany (Siemens, Industry)

September 2007

Summary

The aim of this project is to assess the influence of bone microarchitecture on the mechanical performance of bone and to quantify its changes in microgravity condition as well as in osteoporotic patients on Earth. For this purpose 3D imaging techniques of trabecular bone including micro-CT, pQCT and CT as well as MRT are utilized and new computational and visualizing tools are being developed and employed.

A testing chain is established starting from micro-CT imaging of trabecular bone, building a plastic model of the bone using Rapid Prototyping and, finally, mechanical testing the model. Using Rapid Prototyping as an alternative to Finite Element modelling has the advantage of avoiding all the insecurities of computational approaches at large deformations close to the fracture event. In comparison to mechanical tests on real bone, the advantages are that the material properties are fixed and that identical copies are tested more than once under different loading conditions.

Bone microarchitecture from three different skeletal sites vertebral body L3, proximal tibia, and distal tibia is or will be investigated. This includes bone specimens, in-vivo patients' and, if available, astronauts' data. In addition to the structural measures developed in Phases I and II of this Project, new types of measures based primarily on mechanical considerations are being developed. Predictive power of these measures will be compared with results provided by the testing chain described above.

In addition, the project aims to go beyond a "statical" towards a "dynamical" description of bone failure and architectural changes. We will study the possibility of monitoring and acquisition of time series of 3D micro-CT data from trabecular bones and plastic models during deformation until fracture. The influence of bone remodelling on structural stability is investigated by computer simulation. All aims are supported by the development of new 3D quantitative visualization tools.

Moreover, the Project further develops ultrasound approach for quantification of trabecular bone structure.

Table of Content

Focus and Results of the Current Phase in Brief

- Collection of sets of bone specimens including lumbar vertebral bodies L3 and entire tibiae;

- Imaging of bone specimens with conventional x-ray, computed tomography (CT), and 3D peripheral quantitative CT (3D-pQCT);

- Recruiting of healthy volunteers and osteoporotic patients for magnetic resonance imaging (MRI);

- Development of a testing chain including micro-CT imaging of trabecular bone, building of its plastic model using Rapid Prototyping, and mechanical testing of the model by using both simulated test structures and bone micro-CT data;

- Initial analysis of 3D-pQCT data acquired in-vivo from patients suffering from a ligament rupture, or a fracture of the extremity, or hemiplegic patients as a part of ADOQ study; the trabecular structure is assessed by both the measures of complexity developed during the Phase I and II of the Project and by morphometric parameters.

- Study of the minimal resolution / voxel size of the 3D CT data required for assessment of trabecular bone structure with structural measures of complexity.

- Development and evaluation of a mean-field approach based on mechanical assessment of nodes in a cellular structure in order to evaluate trabecular bone architecture;

- Development of a lattice-dynamics based approach to predicting deformation localisation in cellular solids and trabecular network;

- Assessment of computer simulations of bone remodelling with increased turnover and characterization of the dynamical changes in bone architecture;

- Developing 3D image processing and visualization tools for quantitative analysis of changes in micro-architecture; establishing a method for architectural decomposition of 3D trabecular bone structure;

- Further development of ultrasound approach including:

  - Extension the method of ultrasonic measurements in proximal tibia developed during the Phase II of the Project onto the distal tibia;

  - Study of new ultrasonic testing modalities potentially applicable for assessment of changes in the trabecular bone structure in the proximal and distal tibiae;

  - design of corresponding experimental ultrasonic instrumentation;

1. Collection of 3D data on Microarchitecture from Bone Specimens and Patients

1.1 Bone Specimens

Collection of bone specimens. During a period of four months (from March till June 2007) six sets of specimen were collected by ZMK, Charité – CBF in collaboration with Prof. Gottfried Bogusch, Anatomical Institute of Charité – Campus Mitte, Berlin, Germany. Each set of bone specimens was harvested from the same donor and included lumbar vertebra L3 extracted at the level of the intervertebral disks (cut through the intervertebral disks) and the entire left tibia. The donors' bodies were not frozen at all and were kept at temperature of about 0°C before the extraction of the tibiae and vertebral bodies. The harvested specimen were stored in wet cloth and wrapped inside plastic bags. After the transfer of the specimens to ZMK the bones were immediately put into plastic bags containing sodium chloride. The air was removed (not evacuated) and the plastic bags were sealed. Subsequently the bags were kept in a fridge with the temperature near 0°C.

The collection of specimens lasted longer than expected since it was difficult to have access to human material. We appreciate the great support we received from Prof. G. Bogusch, Charité – Campus Mitte, and his team. Prof. Bogusch himself extracted and prepared the specimens and made all possible efforts providing the project with this valuable bone material.

We were looking for specimen to be harvested from donators without any osteoreactive disease. Despite the fact that the information derived by the death certificates is rather limited, many diagnoses were identified, as it is summarized in Table 1.1. Unfortunately, three donors were suffering from carcinomas which often may induce osteoblastic or osteolytic metastases. Nevertheless we imaged all sets of specimen using the procedures and modalities described below.

Lumbar Vertebrae:

- – Conventional x-ray imaging in two levels (anterior-posterior and lateral)
- – Computed Tomography (CT) including both an acquisition of the entire volume of the vertebral body and three CT images with slice thickness of 1, 2, and 3 mm obtained in sequential mode.

Table 1.1. Clinical diagnoses of the donors indicated by the death certificates.

Age	Sex	Clinical diagnoses
72	f	Tumor cachexia, bronchial-carcinoma
82	f	Mamma-carcinoma, hypertension, depression, pacemaker.[*]
84	f	Cardiac shock, myocardial infarction of the posterior wall, rectum-carcinoma, endometrial-carcinoma
85	f	Pneumonia, lung edema, cardiac insufficiency
86	f	Multiple organ failure, septic-toxic shock, diverticulosis with sigma-perforation, small intestine ischemia
88	f	Cardiac arrhythmia, chronic. cardiac insufficiency, diabetes mellitus

[*] Osteoblastic metastases were found in the vertebral body during CT evaluation.

<u>Tibiae:</u>

- − Conventional x-ray imaging in two levels (anterior-posterior and lateral)
- − CT of proximal tibia: sequential acquisition of three CT-images with slice thickness of 1 mm, 2 mm, and 3 mm in the region defined in Final Report Phase II, 2006.
- − 3D peripheral Quantitative Computed Tomography (3D-pQCT): acquisition of a standard volume at distal tibiae and a volume at proximal tibiae according to the region evaluated with the CT.

As it is shown in Table 1.1, we were able to detect only one set of specimen with osteoblastic metastases in the vertebral body. No metastases were found in the other five sets of vertebral and tibial specimens.

Computed Tomography. The CT was performed according to the protocol defined during the Phase II of the Project (Final Report Phase II, 2006). A CT-scanner Somatom Volume Zoom (Siemens AG, Germany) was used. The following parameters for sequential and helical image acquisition were used: 120 kV, effective 120 mAs, collimation of 0.5 mm, rotation time of 0.75 sec, kernel B45s middle, FOV 228 (512 x 512 pixels image matrix), in-plane pixel size of 0.45 mm.

The **vertebrae** were aligned axially according to anterior-posterior and lateral topograms. The gantry tilt and the location of the transaxial central slice were determined using a bisecting line between the upper and lower endplate of the vertebral body in lateral view (Fig. 1.1). At this position a single slice CT was performed using the slice thickness of 1 mm, 2 mm and 4 mm. Exactly the same set of parameters was used to perform a helical CT of the entire volume of the vertebral body which was reconstructed with slice thicknesses of 1 mm and 2 mm.
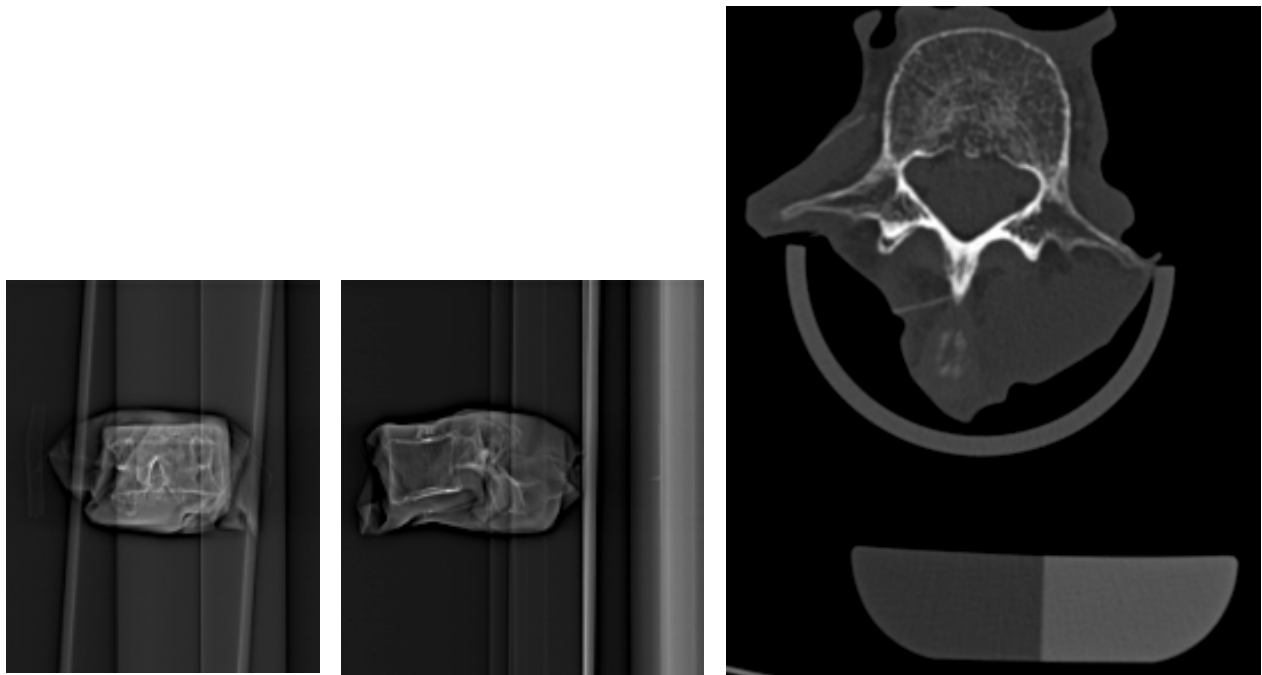

Figure 1.1 CT imaging of lumbar vertebra L3: anterior-posterior topogram (*left*); lateral topogram (*middle*) and 1 mm thick axial slice obtained in sequential mode (*right*). Calibration phantom scanned together with the bone specimen is used for quantitative evaluation of the bone structure including the calculation of structural measures and bone mineral density BMD.

The **tibiae** were aligned axially by using of anterior-posterior and lateral topograms. In order to standardise this positioning protocol we defined that the tibia is placed "axially" if the articular surface of the tibia plateau (lateral and medial condyle) was aligned horizontally. The gantry was tilted according to the lateral view of the tibia plateau and a line was positioned on top of the tibia plateau in anterior-posterior direction. The gantry was positioned 17 mm distal to this line (lateral view) and axial CT slices with thicknesses of 1, 2 and 4 mm were acquired in sequential mode.

All acquired CT-images were transferred to the Project server where they are available for all Project's teams.

3D peripheral Quantitative Computed Tomography. The high resolution 3D peripheral Quantitative Computed Tomography (3D-pQCT[1]) scanner XtremeCT (Scanco Medicals AG, Switzerland) is able to acquire in vivo 3D images of human extremities. It is capable to image and analyze a bone volume of about 9 mm with an isometric resolution of 82 μm. During a period of three minutes 110 CT slices along the longitudinal axis of the bone are acquired simultaneously. The device is usually used for in vivo measurements of peripheral bones in patients' arms and legs. The scanner's software performs densitometry and bone morphology evaluation and calculates e.g. the following parameters: cortical and trabecular bone mineral density (BMD), bone volume fraction BV/TV, trabecular number Tb.N, trabecular thickness Tb.Th, trabecular separation Tb.Sp, and inhomogeneity of the trabecular network.

The standard measurement at **distal tibia** is located 22.5 mm proximal of the articular surface of the upper ankle joint. Following this standard procedure for patients, 3D-pQCT data were acquired from the six collected tibial specimens using the standard control file for left tibiae (TL). As the in vivo positioning protocol requires fibula and talus, we additionally performed a lateral scout view to substitute the missing information required for positioning of the reference line.

There is no standard 3D-pQCT procedure for **proximal tibia**. Currently, in-vivo measurements in proximal tibia are not possible. The following procedure was developed to image the proximal tibia of bone specimens. The tibial specimens were place inside the scanner with the proximal part ahead and supine. They were aligned axially according to anterior-posterior and lateral scout views. To standardise this positioning protocol we defined the tibia to be placed "axially" if the articular surface of the tibia plateau (lateral and medial condyle) was aligned horizontally, similarly as it was defined for the CT imaging. The acquired volume included 110 slices and it began at 12.5 mm distal of the reference line positioned through the tibia plateau. Although it is not possible to tilt the gantry of the 3D-pQCT scanner, the acquired volume includes, due to its large extent, the smaller standardized region (Final Report Phase II, 2006) imaged with the conventional CT; same region is also analyzed with the developed ultrasound technique (Sect. 7).

Segmented 3D-pQCT reconstructions of distal and proximal tibia of the same donor are shown in Fig. 1.2. All acquired images and the results of their evaluation were transferred to the Project's server and made available to all partners. At the time of the report the evaluations of the 3D-pQCT images is work in progress, the obtained results are preliminary and have to be validated.

After the imaging with conventional x-ray, CT, and 3D-pQCT, the collected tibial specimens were sent to the partner RTU for ultrasound examination (Sect. 7) and then together with the vertebral specimens all bone samples were shipped to the partner LBIO were the specimens will

---

[1] Both the partner CBF and ADOQ study team (see Sect. 1.2) use another abbreviation for this scanner, 3DpQCT. The abbreviation 3D-pQCT is already established in scientific publications (Milos et al. 2007, Milos et al. 2005, Pistoia et al. 2004). For that reason, the Project Coordinator PS has chosen the convention 3D-pQCT for use in the present Report.
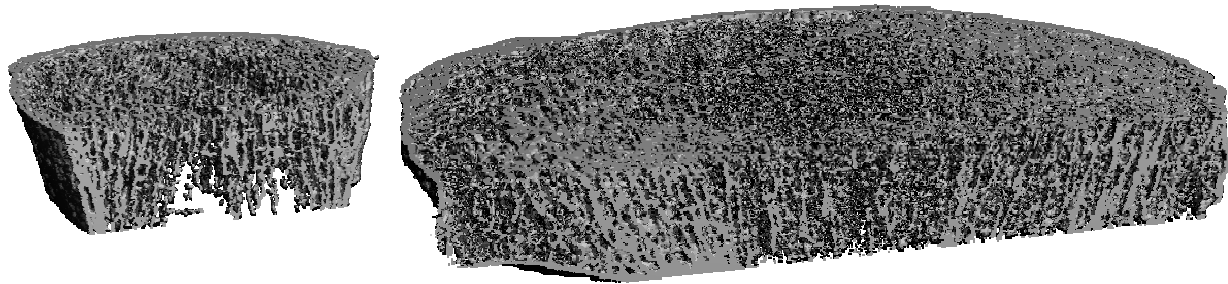
Figure 1.2 3D reconstruction of bone architecture in distal (*left*) and proximal (*right*) tibia of the same donor whose vertebral body L3 is shown in Figure 1.2.

be cut initially with a hand saw and then with Buehler IsoMet 1000 (Buehler GmbH, Düsseldorf, Germany) precision sectioning saw specially obtained for the Project.

1.2 Data from Patients

Data from ADOQ study. Advanced Detection of Bone Quality (ADOQ) is a study funded by European Commission under Contract QLK-CT-2002-02363, Key action No. 6, "The aging population and disabilities", and co-funded by Swiss government and the ESA. In this framework different subject groups were investigated in order to develop reference data for the described above 3D-pQCT scanner XtremeCT, Scanco Medical AG, Switzerland. In ADOQ study the task of the CBF was to collect 3D data from patients suffering from a ligament rupture, or a fracture of the extremity, or hemiplegic patients. In the Project being reported one of the CBF's tasks was to provide the partners with 3D-pQCT images from the ADOQ study.

For each patient the 3D-pQCT investigations were performed over a period of six months including baseline imaging and four follow-up measurements with an interval of 6 weeks. The measurements were performed at all extremities: left and right distal radii and distal tibiae (Fig. 1.3). Altogether seven volunteer patients were examined: two patients followed the protocol and completed all five visits, two patients participated in four visits, one patient allowed 3 follow-up investigations, and for two persons only visits were completed. Table 1.2 summarizes the diagnoses for the participating patients.

The in vivo 3D-pQCT measurements are high frequently affected by movement artifacts. These artifacts influence the derived bone structure evaluation results and can even make the evaluation impossible. That was a severe problem when radii were imaged in vivo: we were able to obtain only one set of five follow-up radius measurements where movement artifacts were small; all other 3D data suitable for evaluation were obtained from distal tibiae.

Whether in vivo images containing such movement artifacts can be used for quantitative evaluation will require further investigation.

Only thoroughly checked 3D-pQCT images of a high quality were transferred to the Project server. At the time of the report the evaluations of the 3D-pQCT images acquired in vivo is a work in progress and the obtained results are preliminary and have to be validated.

Table 1.2. Clinical diagnoses of the patients agreed to participate in the ADOQ study.

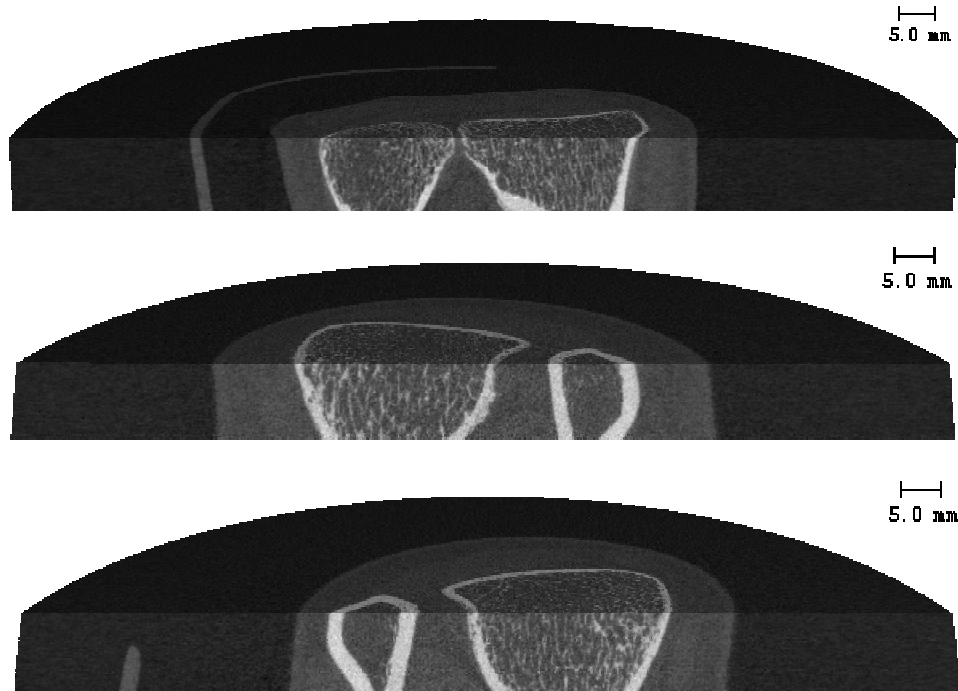| Patient No.	Clinical diagnoses
1	Fracture at the tibia plateau, left side
2	Fracture of the calcaneus, left side
3	Fracture of the femur, left side
4	Fracture of the humerus, right side
5	Fracture of the pelvis, left side; fracture of the prox. radius, left side
6	Hemiplegy, left side
7	Rupture of a ligament at the knee, left side

8

Figure 1.3. Non-segmented 3D views of bone structure reconstructed from the 3D-pQCT images obtained in vivo: a standard region in the left distal radius (*top*), standard regions in the left distal tibia (*middle*) and right distal tibia (*bottom*) obtained from the same patient during one visit. Voxel size is 82 μm.

Preparation to acquire MRI data from normal volunteers and osteoporotic patients. Ethics Committee Application for examination of patients by magnetic resonance imaging (MRI) was prepared and submitted by the LBIO team. Positive decision of the Ethics Committee was obtained in August 2007. LBIO team prepared an information sheet for patients participating in the study.

Till now 12 patients agreed to participate in the study organized at the 4th Medical Department of Hanusch Hospital, Vienna, Austria. Six of the volunteers have no osteoporosis and six of the patients have osteoporosis as diagnosed by DXA bone mineral density measurements. The data acquisition will be performed on the newly installed Philips Achieva 1.5 Tesla MRI scanner.

Our first evaluation of trabecular bone in spine by MRI showed that the resolution of the trabecular structure in vertebral body was below the expected resolution. Therefore, technical support will be provided from Philips to adjust the MRI device in order to improve image resolution with the microscopic coil up to isotropic voxel size of about 120 μm.

In parallel to spine, we plan to scan the smaller tibiae and finger bone of patients, what might give data with better resolution of the trabecular bone structure.

2. Production and Test of Resin Models Manufactured by Rapid Prototyping

In order to study a mechanical performance of trabecular bone architecture the Project requires establishing a testing chain which consists of three steps:

- − micro-CT (µCT) imaging of trabecular bone,
- − building a plastic model of the bone using Rapid Prototyping (RP) machine,
- − mechanical testing the model on material testing machine.

Using Rapid Prototyping as an alternative to Finite Element modeling has the advantage of avoiding all the insecurities of computational approaches at large deformations close to the fracture event. In comparison to mechanical tests on real bone, the advantages are that the material properties are fixed and that identical copies will be tested more than once under different loading conditions.

2.1 Rapid Prototyping System

MPICI has two Rapid Prototyping machines available at the Department of Biomaterials: digital light processing (DLP) machine Perfactory® Mini SXGA Multi Lens (Envisiontec GmbH, Gladbeck, Germany) and Solidscape® T66 Benchtop molten wax 3D jet plotting machine (Solidscape, Inc., Merrimack, USA). Preliminary experiments showed that the strength of wax-based models is too weak for available testing machines, the resolution of the 3D wax plotter is smaller than the one of the DLP machine (smallest achievable voxel size 76 µm × 76 µm × 13 µm versus 25 µm × 25 µm × 25 µm for DLP system) , and wax plotter requires much longer time to build the model. Thus, we selected DLP Perfactory® Mini SXGA Multi Lens (Envisiontec GmbH, Gladbeck, Germany) Rapid Prototyping machine for further experiments.

The Perfactory machine is shown in Figure 2.1. Digital light processing system of type Direct Light Projection System is located inside the gray base which has a glass window above the lens system of the projector. On top of the base above the window there is a polymerization
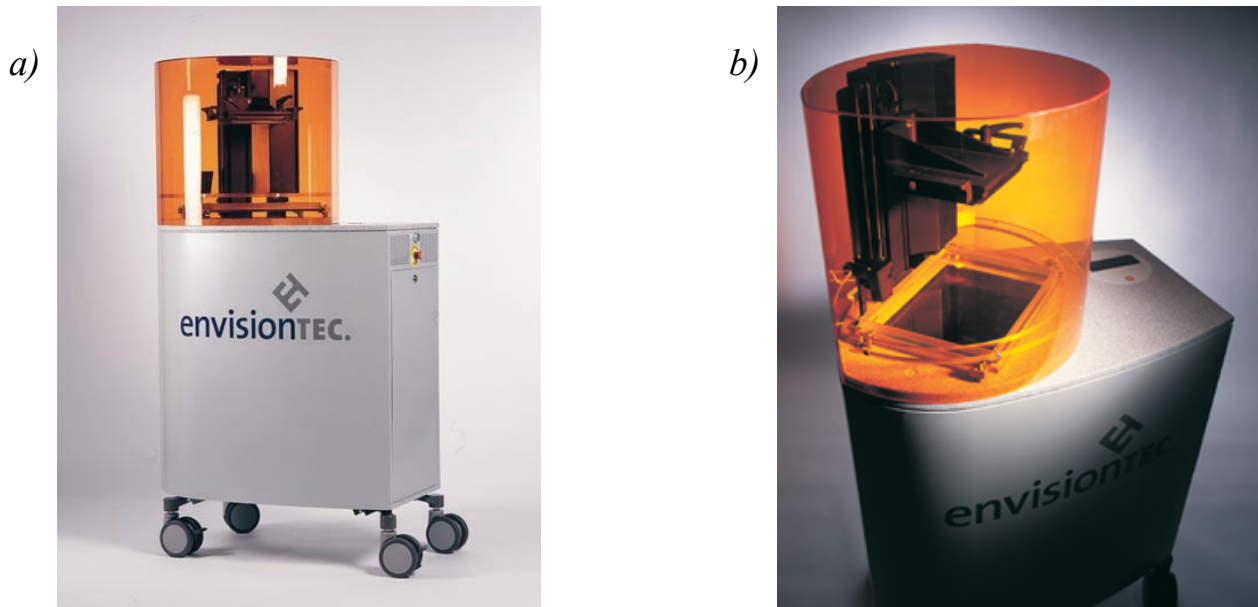
a)

b)

Figure 2.1. Perfactory® Mini SXGA Multi Lens Rapid Prototyping machine (Envisiontec GmbH, Gladbeck, Germany). Front view *(a)* and a view from above *(b)*.

basement filled a liquid photosensitive polymer. A moving black horizontal building platform is attached to the vertical support system at the rear part of the system. Movable amber light hood protects the system from exposure by parasite light and dust. Control panel is located on the right part of the upper surface of the system base.

The principle of these systems is depicted in Fig. 2.2: a digital mirror device or a dynamic liquid crystal display mask is used to control the exposure of photosensitive polymer with visible light. Each layer of the virtual 3D model to be built is projected via the mirror onto a thin layer of photopolymer, which solidifies, where it is exposed, and remains liquid, where not. After exposure, the z-stage moves up a layer thickness, and the process is repeated until the constructed part is complete. Thereafter, remaining liquid polymer is washed off.

The advantages of this technique are high building speed and low cost per volume, the drawback is the fact that one is restricted to a limited amount of photosensitive polymers developed for these systems. The achievable resolution and the maximum built area are inversely proportional to each other, because of the fixed number of pixels of the mirror or of the mask (Bertsch et al 1999).
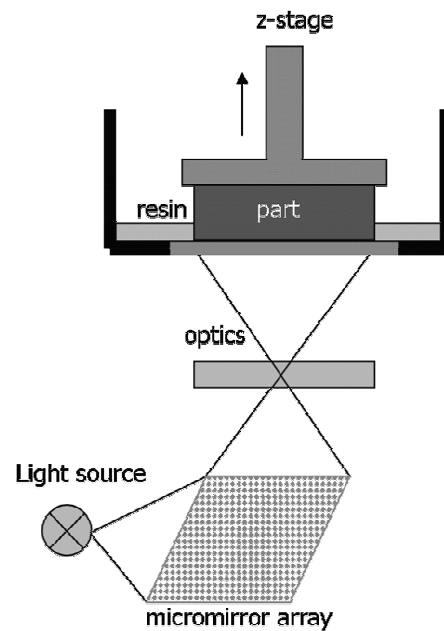

Figure 2.2. Scheme of Rapid Prototyping by digital light processing using Direct Light Projection System

The layer thickness or vertical voxel size of the available Perfactory® Mini SXGA Multi Lens system is either to 25 µm or 50 µm. To get smallest possible voxel size the layer thickness of 25 µm was selected. The building envelope $x \times y \times z$ depends on selected in-plane voxel size and is either

- 42 mm × 34 mm × 230 mm at voxel size 32 µm × 32 µm × 25 µm or
- 32 mm × 26 mm × 230 mm at voxel size 25 µm × 25 µm × 25 µm.

Size of the Perfactory® Mini SXGA micromirror array which defines the number of pixels in one constructed layer is 1280 pixels × 1024 pixels (Envisiontec 2006).

2.2 Optimal Approach to Convert Micro-CT Data to the Format of Rapid Prototyping System

Standard input data for RP machines are triangulated surfaces of the object to be built stored as STL-file, here STL is abbreviation of standard triangulation language. The data produced by µCT-scanners are 3D matrix of voxels representing the x-ray attenuation. The µCT-image stores the linear attenuation coefficient using two bytes or 16 bits per voxel; depending on the model of the scanner 12 to 16 bits or these two bytes are used. Following the standard procedure it is necessary to construct a triangulated surface of trabecular bone from the voxel data acquired by the µCT. This transformation requires finding optimal thresholding procedure for data binarization and cumbersome choice of the triangulation parameters. Beside the time required to find optimal transformation parameters the calculation of triangulated surface itself is a time consuming task. Moreover, after the surface is constructed, the manipulation of the data like artificial disconnection of trabeculae or simulated thinning of the trabeculae is not possible any more. Before the model of the trabecular bone can be build by the RP-machine the STL-data

should be converted back to the voxel data of appropriate for the machine x-, y-, and z-sizes by the special RP-software and put into so-called job-file (which is zip-archive) as a sequence of the slices saved as grayscale 8 bits per pixel palette PNG-file. The reverse transformation from triangulated surface into the voxels of a specified geometry is also a time consuming process.

The team developed another approach to prepare and convert µCT-data into the format appropriate for RP-machine. It is based on the direct resampling of the µCT-data to the geometry required by the RP-system without intermediate transformation to and from triangulated surface. The approach consists of the following steps:

1. Casting of the data to 1 byte/voxel.
2. Resampling of the data to geometry required by the RP-system.
3. Binarization of the data.
4. Saving the 3D volume as a stack of PNG-images and final adjustment (padding of the image to the matrix of the RP-machine and appropriate naming of the files).

The processing of the data is performed by using the Amira 3D visualization and processing software platform. Initially the data were processed and prepared manually, and after the development of the approach had been completed a special RP-module for Amira was designed.

Casting of the data is required as the 3D µCT data have bit depth of 16 bits/voxel while the RP-system requires 8 bits/voxel slices. It also reduces by two times the size of the processed data. The interval of original attenuation values to be converted into 8 bit/voxel representation (that are grayscale values in the interval from 0 to 255) was defined using the histogram of attenuation within the processed 3D volume. As the coefficient of attenuation of the air is usually around 0 in units of µCT image, the negative attenuation values can be omitted. Outliers and artifacts with extremely high attenuation can be also avoided by specifying the upper attenuation limit A_{max} which could be set using the attenuation histogram. The casting of voxels values from 16 bit/voxel A_{16} to 8 bit/voxel A_8 is performed using the Amira Arithmetic module code

$$A_8 = A_{16}*(255 / A_{max})*(A_{16} > 0)*(A_{16} <= A_{max}) + 255*(A_{16} > A_{max}) . \qquad (2.1)$$

Resampling to the geometry required by RP-system. Let us assume that the micro-CT data have a size of $n_x \times n_y \times n_z$ pixels and cubic voxel size of λ^{CT} µm, while RP-system requires the data slice of geometry $l_x \times l_y$ voxels, in-plane voxel size $\lambda_x^{RP} \times \lambda_y^{RP}$ µm, $\lambda_x^{RP} = \lambda_y^{RP} = \lambda_{x,y}^{RP}$, and slice thickness or voxel height of λ_z^{RP}. In general case, RP systems have non-cubic voxels for which the vertical z-size (or height) of the voxel λ_z^{RP} is not equal to its in-plane xy-size $\lambda_{x,y}^{RP}$.

The resampling coefficient in xy-direction c_{res} is defined as

$$c_{res} = \frac{l_x}{n_x} = \frac{l_y}{n_y} , \qquad (2.2)$$

and the scale M of the built model relatively to the original data is

$$M = \frac{l_x \lambda_{x,y}^{RP}}{n_x \lambda^{CT}} = \frac{l_y \lambda_{x,y}^{RP}}{n_y \lambda^{CT}} = c_{res} \frac{\lambda_{x,y}^{RP}}{\lambda^{CT}} \qquad (2.3)$$

In the reverse situation when the desired scale M of the plastic bone model is specified from the beginning, then the resampling coefficient can be calculated as

$$c_{\text{res}} = M \frac{\lambda^{\text{CT}}}{\lambda_{x,y}^{\text{RP}}}, \text{ and } l_x = c_{\text{res}} n_x, \quad l_y = c_{\text{res}} n_y. \tag{2.4}$$

Finally, the number of layers in the model which is also the number of non-cubic voxels in vertical z-direction is defined as

$$l_z = c_{\text{res}} \frac{\lambda_{x,y}^{\text{RP}}}{\lambda_z^{\text{RP}}} n_z . \tag{2.5}$$

Thus, the target size of the required image matrix is derived and the resampling of the 3D µCT data of size $n_x \times n_y \times n_z$ should be performed to the new size of $l_x \times l_y \times l_z$. The experiments have shown that the optimal algorithm for the resampling is based on a Lanczos kernel (Final Report Phase I 2003, Lehmann et al 1999) which is implemented in Amira.

Binarization of data is performed using global thresholding. The threshold is defined from the attenuation histogram. Marrow voxels are represented by voxel value 0, while bone voxels have voxel value set to 255. This is the requirements of the RP-system that voxels to be solid should have its value set to 255 and the empty voxels should have 0 values. The resulting 3D volume of binarized voxels is then saved as a stack of PNG-files.

Final adjustment includes optional padding, optional adding of endplates, and compulsory renaming of the resulting files accordingly to the requirements of the RP-system.

- It might be necessary to pad or add margins to each image in the created stack of the PNG-files to the size of the RP-image matrix if the target geometry in the resampling procedure was selected smaller then the RP-matrix size. The padding could be performed either manually using batch processing by ImageMagick® image processing software (ImageMagick Studio 2007) which is freely available under GPL license or by the specially developed Amira RP-module (Sect. 6.1). For testing the strength of the plastic trabecular bone models in the material testing machine it might be convenient to have flat endplates attached to the top and the bottom of the bone model. The image representing endplate is simply an additional PNG-slice of the same size like the bone PNG-slices and with all its pixels set to value 255 (white). The number of endplate slices is defined by the desired thickness of the plate and by the vertical voxel size λ_z^{RP} of the RP-system. All PNG-file should be grayscale 8 bit/pixel palette images.

- Finally, all the PNG-images should be named accordingly to the convention used in RP-system. The file names should follow the template `Type`t`_mask_`$nnnn$`.png`. Here t is the either 1 for initial burn-in slices or 3 for all other normal slices. The burn-in slices are initial layers built with longer exposure then normal slices in order to provide stronger base for the model, usually there are 12 to 60 burn-in slices, The slice counter $nnnn$ is the slice number including leading zeros; first slice has number 0, last one has number $N-1$, where N is the total number of the slices to be built.

- The appropriately named PNG-files together with the text file `Job.cfg` describing the parameters of the RP-model and optional text file `Data_Processing_Info.txt` should be packed in ZIP-archive with any meaningful file name and extension "$*$.job". The configuration file `Job.cfg` can be taken from any native job-file generated by the RP Perfactory software. Only the lines contained the number normal model slices N_MODEL_SLICES and number of burn-in slices N_BASE_SLICES should be set to appropriate values so that the $N\_BASE\_SLICES + N\_MODEL\_SLICES = N$. Optional

file `Data_Processing_Info.txt` contains information about the geometrical sizes of the model and software used to prepare the model slice; it can be omitted.

Constructed as described above, job-file is treated as standard RP-file by the Perfactory Software Suite by Envisiontec GmbH (Envisiontec 2006). All parameters in the configuration file and the images of the model slices can be later edited in the Perfactory Job Modifier program. The prepared sliced model can be loaded into the rapid prototyping machine using the Perfactory Direct program and then reproduced in plastic.

The preparation of the data for RP-system accordingly to the developed approach requires about 15 minutes of CPU time on the workstation with Pentium® 4 3.2 GHz and 4 GB of RAM for a µCT vertebral trabecular bone data fragment of size 10 mm × 10 mm × 15 mm at voxel size 38 µm. The time required by the Perfactory RP-system to build a model is defined by the height of the model (number of slices in the model). For the vertebral trabecular bone model mentioned above the built time is about 12 hours. The average built speed which can be used for rough estimation of the time required to build the model is 0.057 mm/min or 2.3 layers per minute.

2.3 Building and Mechanical Testing of Rapid Prototyping Models from Test Structures and Bone Micro-CT Data

During the reporting period of time three types of plastic models were produced by the RP-system: two artificial test structures including simple cubic (SC) and body centred cubic (BCC) 3D cellular structures or grids (Woesz et al 2004), and the model of trabecular bone of human forth lumbar vertebra L4 (see Fig. 2.3). The artificial regular SC and BCC structures were used to establish a standardized procedure and parameters for production, postprocessing and fixation of the RP-models and to develop and check procedure for mechanical compression testing of the RP-models produced by the Envisiontec Perfactory System.

All models were produced from hybrid photopolymer Perfactory R11 (Envisiontec GmbH, Gladbeck, Germany). Mechanical properties of the R11 resin are summarized in Table 2.1 (Envisiontec 2007).
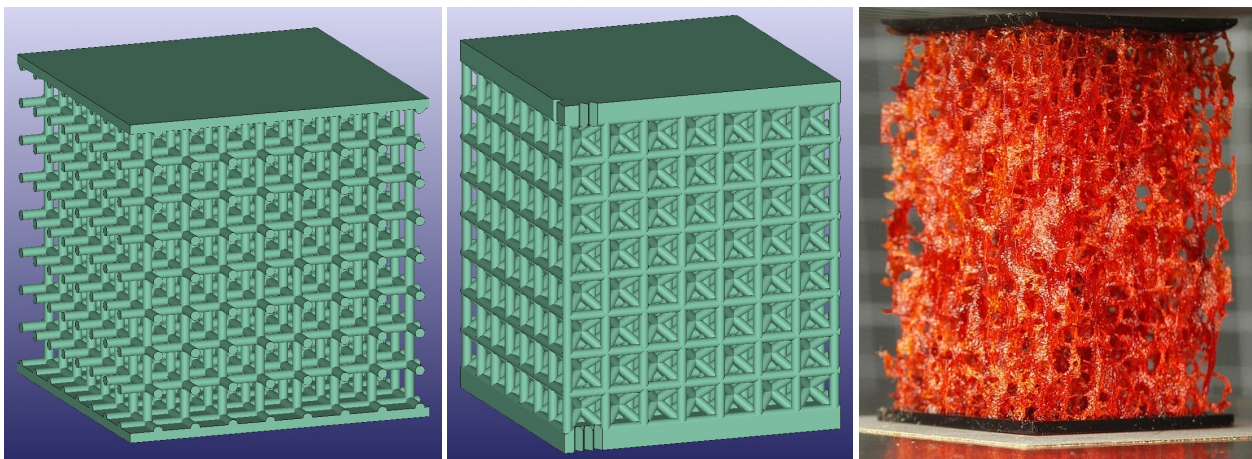

Figure 2.3. Three types of the models used in the initial experiments: simple cubic (SC) (*left*) and body-centered cubic (SCC, *middle*) test cellular structures designed with 3D CAD software, and the RP-model of trabecular bone from central part of human forth lumbar vertebrae L4 (*right*). Model of vertebral trabecular bone was produced directly from the µCT-data (Final Report Phase II, 2006) by using the approach described in Section 2.2. The endplates appropriate for compression strength tests are attached to the top and bottom of the structures.

The performed experiments helped us to establish the following standardized parameters for building, postprocessing and fixation of the RP-model. The optimal parameters controlling the construction of the RP models are: exposure time for burn-in layer is 9500 ms and exposure time for standard layers is 4000 ms, number of burn-in layers is 60. The models were built in the air conditioned laboratory with constant room temperature of 21° C. The standardized postprocessing (cleaning) of the RP-models includes 30 seconds intensive washing in 2-Propanol bath to remove most of the remaining liquid photopolymer and 4 minutes ultrasound bath in 2-Propanol which removes the rest of the non-solidified resin, both performed at room temperature. Bandelin Sonorex RK 31 H compact ultrasonic bath (Bandelin electronic GmbH & Co. KG, Berlin, Germany) with operating frequency of 35 kHz and effective power of 30 W was used for ultrasonic cleaning. After the cleaning, the models were dried with compressed air and fixated for 3 hours in UV-light curing chamber Metalight QX1, with UV-spectrum in range from 320 nm to 400 nm (Primotec, Bad Homburg, Germany), at the temperature of maximal +5° C above the room temperature.

Table 2.1. Mechanical properties of Envisiontec Perfactory R11 polymer (Envisiontec 2007).

Tensile Strength	50 MPa
Elongation at Break	8 %
Elongation at Yield	13 %
Modulus of Elasticity	1245-1510 MPa
Flexural Strength	75 MPa
Flexural Modulus	2450 MPa
Izod Impact-Notched	0.35 J/m
Hardness (Shore D)	85
Water Absorption	0.71 %

The mechanical compression strength tests of the models were performed on universal material testing machine Zwick Z010 (Zwick GmbH & Co. KG, Ulm, Germany). The tests were carried out with compression speed of 5 mm/min and preloading with force of 5 N. The force-displacement curve acquisition parameters: the distance between the samples was not more than 0.1 N and the samples were acquired at least each 0.01 s.

For initial experiments 16 models of the SC structures and 13 models of BCC structures were produced. The original size of the SC model is 32 mm × 32 mm × 34 mm including top and bottom endplates of thickness 1 mm each. The original size of the SCC model was 29 mm × 29 mm × 36 mm including two endplates of thickness 2 mm each. For both structure types the rod thickness was 1 mm, number of unit cells was 7 × 7 × 8. The voxel size of the RP systems was 32 μm × 32 μm × 25 μm. The model of original size occupied most of the building area of the RP system, thus, one model per RP-cycle could be produced. In order to produce four models per one RP-cycle the models were scaled down by factor 2.0 in each direction.

In addition, 12 RP-models of trabecular bone of human lumbar vertebra L4 were built. The model was constructed from μCT-data of normal vertebral bone of specimen 037-99, BV/TV is 13.6 %. The entire vertebral body was scanned with voxel size of 37 μm by our industrial partner Scanco Medical AG during the previous phase of the Project (Final Report Phase II, 2006). A cuboid of size 10 mm × 10 mm × 14.8 mm was selected from the central part of the vertebral body and the RP-job was obtained using the approach described in Section 2.2.

All build models were tested on compression and the maximal stress (strength) of the models was defined as maximal force (first maximum of the force-displacement curve) divided by the cross-section of the model. For each type of the structure the strength of the models was normally distributed accordingly to Kolmogorov-Smirnov and D'Agostino-Pearson (Sheskin 2004) criteria. But the variation of the strength in each group was quite large: relative standard deviation was 15 % for BCC structures and 32 % for SC structure. Relative standard deviation of the strength of the vertebral trabecular bone RP-models was 17 %.

Additional experiments were performed together with the specialists from Envisiontec. They showed that there was a defect in fixation of the mirrors in a light guidance system of the projector that led to the variation of the light intensity in time. In addition, few defective elements in the light processing chip were detected which were responsible for local defects in the model. To cure these problems the entire projector system was exchanged. The project team was also advised to use fresh photopolymer when manufacturing objects with such a fine structure and to increase the size of the built models in order to allocate more voxels in the cross-section of the structural elements. As an alternative, if it is necessary to keep the models small, for example, in order to be able to scan them with high resolution μCT-scanner, the projector system can be adjusted to a smaller *xy*-voxel size.

Using the improved RP-system, five BCC models of the full size 29 mm × 29 mm × 36 mm were manufactured and tested using the protocol described above. The results of the compression strength tests are summarized in Figure 2.4. The variation in model strength became much smaller and its standard deviation is 2.9 % which is more than five smaller than it was before. In addition, Seven BCC models of the scale 1/2 were built. The variation of strength of smaller models is three times larger than the one of the large BCC models; nevertheless its standard deviation is below 10%.

At the time of the report the team manufactures the RP-models of the vertebra in order to obtain enough statistics and estimate the variation of its strength and compare it with the difference in strength between normal, osteopenic, and osteoporotic bone structures.

At present we also make experiments with building two vertical supporting walls at opposite sides of the bone area which unload and possibly protect bone elements during the construction of the model by RP-machine (Figure 2.5). Five such models were built. The supporting walls were removed before compression strength tests by using precise micro band saw PROXXON MBS 230/E (PROXXON GmbH, Niersbach, Germany). First mechanical testing results showed no significant improvement in the model strength, and our preliminary conclusion is that such additional supporting elements are not necessary.
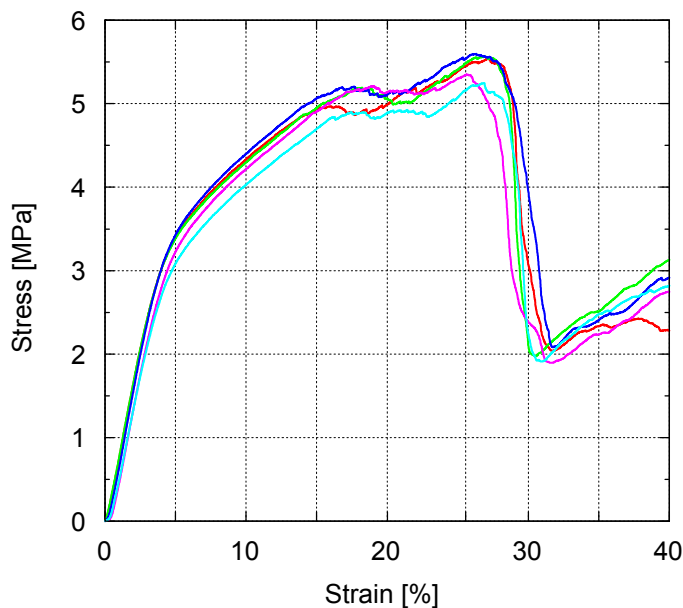

Figure 2.4. Strain-stress curves for compression loading obtained for five models of the BCC cellular structure. Different colors represent the results of testing of different models.

Figure 2.5. Model of trabecular bone of forth human lumbar vertebra L4 with two additional vertical supporting walls which make the model more stable and unload bone elements during building it by RP-machine.

16

3. Quantifying the Microarchitecture with Existing Measures and Correlating with Mechanical Test on the Models

3.1 Data and Methods

Based on the ADOQ study, 3D-pQCT data of distal tibia was available for the structural quantification of the microarchitecture. The data were acquired in-vivo by XtremCT 3D-pQCT scanner (Scanco Medical AG, Switzerland) from one patient with a knee band rupture and thus a knee fixation. Four pQCT images with voxel size of $82\,\mu m$, image matrix of 1536 voxels × 1536 voxels × 110 voxels (length of the imaged region 9.02 mm) were scanned with interval of six weeks starting from the day of trauma, i.e. the four pQCT images represent changes in time of the trabecular bone structure in the distal tibia.

The pQCT images were converted from 3D-pQCT data format into the 3D mesh format and loaded into the Amira software platform.

For the quantification of the bone microarchitecture we focus only on the trabecular part of the bone. Therefore, to separate the trabecular bone from the rest of the imaged 3D data we build volumes of interest (VOI) using the image segmentation module of Amira. Then, in order to reduce the level of noise in the pQCT data they were filtered using a 3D median filter. Bone and marrow voxels were separated by using of a global thresholding; the threshold level was set to 2800 units of the pQCT image.

At first, we calculated the bone volume fraction BV/TV which provides the information about the amount of bone material. Then we calculated the most interesting of the introduced structural measures of complexity (SMCs), which base on symbol encoding, curvature, translational invariance and local shape of trabecular bone elements (Final Report Phase II, 2006).

SMCs based on symbol encoding were introduced and described in Final Report, Phase II, 2006 and in Saparin et al. 2005:
– 3D Normalized Entropy S_n of geometrical locations of bone tissue,
– Structure Complexity Index, SCI $_{BV/TV}$, based on bone volume fraction,
– 3D Structure Complexity Index, SCI_{3D},
– Surface Complexity Index (SurfCI) and Surface Index of Global Ensemble (SurfIGE).

Measures based on local shape and curvatures. Shape based SMCs characterize the mean shape of the trabecular structures and their variability over the analyzed 3D volume (Marwan et al., 2005):
– Shape Complexity (SHC) and the Averaged Shape Index (ASHI),
– Shape Mutual Information (MISH) are able to quantify the variety of different shapes,
– the Marching Cubes Entropy Index (MCE) and
– the Marching Cubes Complexity (MCC), which quantifies the complexity of the bone surface,
– total curvature K and mean curvature H.

Measures assessing translational invariance. These measures based on fractal properties and translational invariance (Marwan et. al, 2007):
– Lacunarity,
– Morans's I index.

The SMCs are calculated on the trabecular bone of the distal tibia within the specified VOI. As the same bone region was scanned at six weeks intervals, for the first time the results allow us to study the structural change in the same trabecular bone over time.

3.2 Preliminary Results

The bone volume fraction BV/TV confirms the bone loss after trauma due to the fixation of the lower extremity (Figure 3.1). Shortly after the trauma, the BV/TV was more than 46% in the entire bone VOI and more than 31% in the trabecular bone VOI. After 18 weeks, the BV/TV decreased to a value below 42% for the entire bone and to 26% for trabecular bone which is a loss of more than -15% of its initial value. That corresponds roughly to a dramatic bone loss in the trabecular part of almost -1% per week. Unfortunately the details of the therapeutic treatment protocol are not known at the moment of time; the reduced bone loss after eight weeks could refer to the therapy and, thus, could possibly explain a non-linearity in decreasing of the BV/TV. The relative change of the bone loss computed from spline fitted data reveals an increasing bone loss in the first eight weeks, up to a relative change of almost -0.8% per week (entire bone) and -1.5% per week (trabecular bone). After this time, the bone loss decreases and is finally only -0.5% per week and -0.7% per week, respectively.

The Structure Complexity Indices SCI_{3D} and $SCI_{BV/TV}$ reveal a decrease of the structural complexity of the trabecular bone microarchitecture (Fig. 3.2), and, hence, confirm previous findings (Saparin et al., 2005). The decrease in 18 weeks is -6% for SCI_{3D} and -3% for $SCI_{BV/TV}$. When comparing these results for complexity indices with the range of change of other parameters we should take into account that these are logarithmic measures. The SMC measure SurfIGE exhibits the same behaviour (but with contrary sign). It increases about 8%.

The Surface Complexity Index SurfCI also shows a decreasing complexity of the bone architecture over the time. However, it slightly differs from the SCI measures. Whereas the other measures show more or less linear behaviour, SurfCI has a more nonlinear decrease with bone loss, revealing a rapid decrease in the beginning and then a more moderate decrease. Its decrease over the 18 weeks is -3% in average.
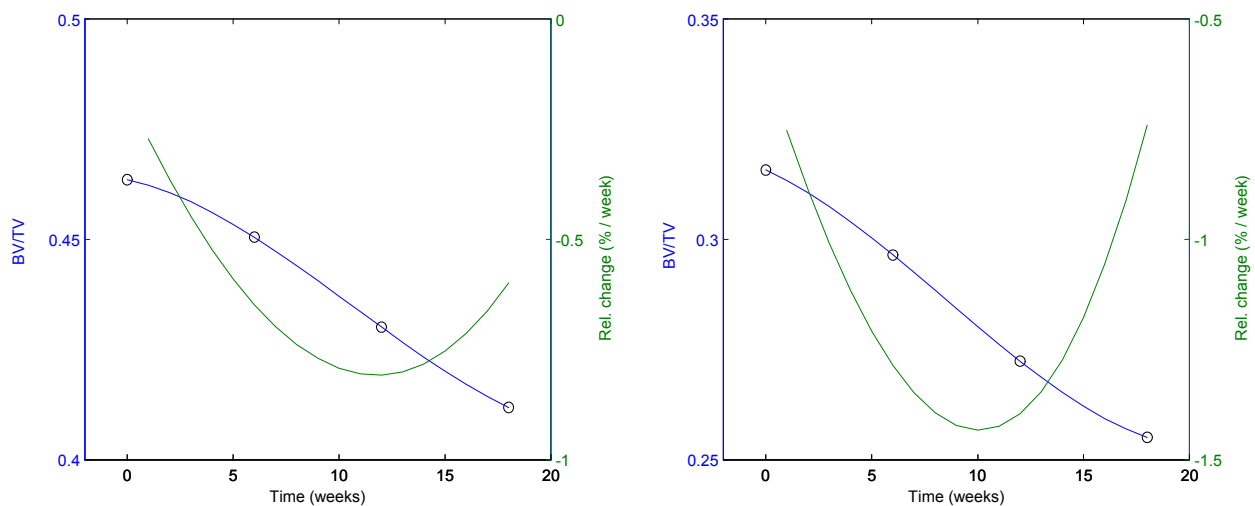

Figure 3.1.: Bone volume fraction BV/TV (*blue line*) and the rate of bone loss (relative change of BV/TV, *green line*) during 18 weeks after band rupture trauma for the entire bone (*A*) and for the trabecular bone VOIs (*B*). The rate of bone loss changes from moderate to dramatic during the initial weeks, and, after 10 weeks, back to a moderate bone loss.
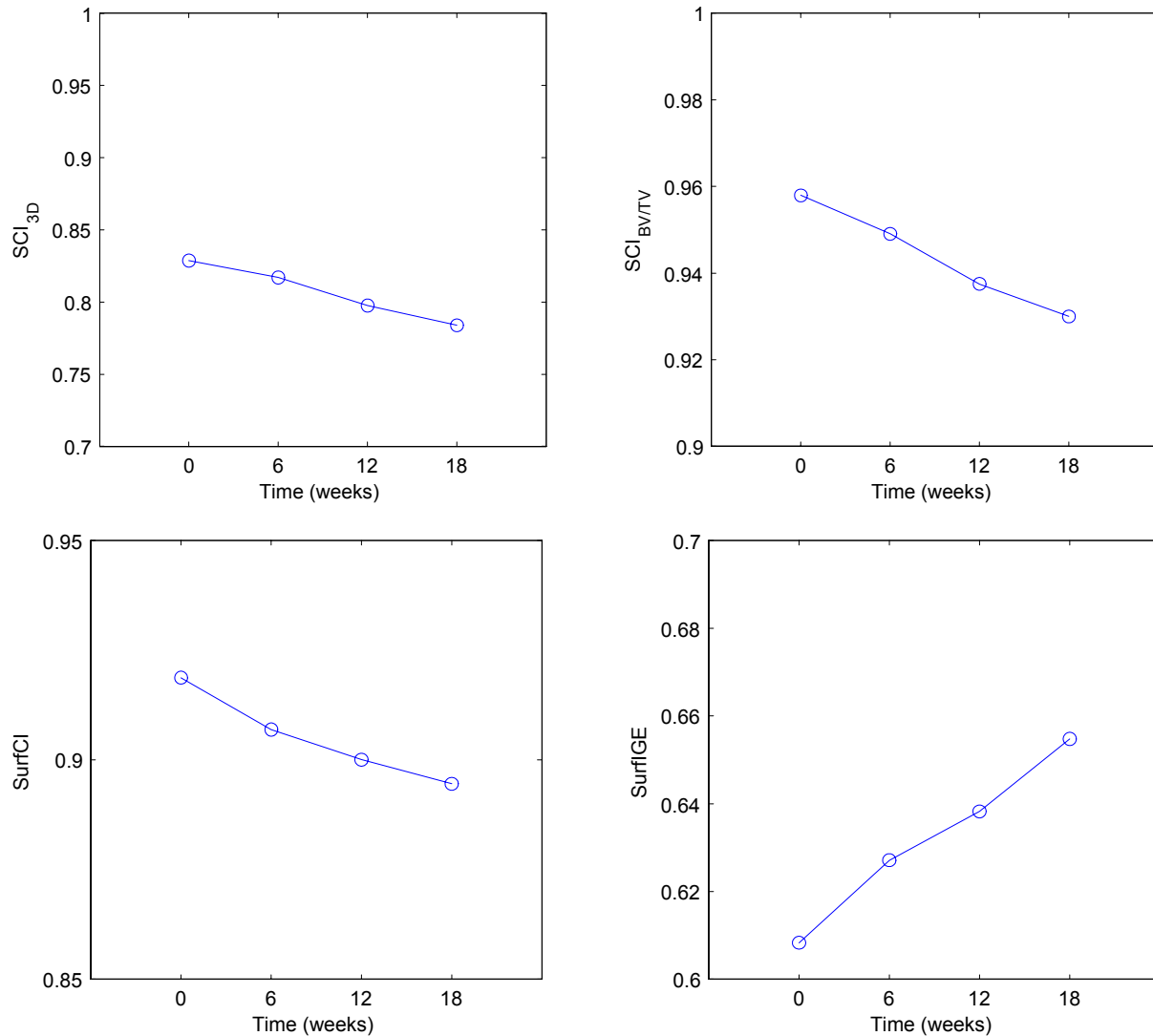
Figure 3.2. Changes of symbol-encoding based structural complexity measures during 18 weeks after band rupture trauma for the trabecular bone VOI.

The entropy of geometrical locations S_n decreases for the first 12 weeks, but then increases again, indicating that the complexity of the trabecular microstructure is again increasing after starting exercises. However, the change in this measure is rather low (0.3%). Therefore, this result is not yet really reliable and still needs further investigation using additional samples.

Shape-based measures are based on a totally different approach and do not utilize symbol-encoding. The shape-based SMCs also show a change in the complexity of the microarchitecture during immobilization and treatment (Fig. 3.3). The Averaged Shape Index ASHI is larger than 1, indicating a presence of a large amount of convex structures. Within the 18 weeks, this value slightly increases, what is in agreement with the findings for proximal tibia reported in the previous project phase (Final report Phase II, 2006). The increase may be a hint for a reduction of connected structures or a possible transition from plate-like to more rod-like structures.

The Shape Mutual Information MISH reveals a dramatic change of the variety of trabecular structures within the first six weeks: the variety of the different shaped structures, like plates, rods and connected trabeculae, reduces within this time (perhaps toward only rod-like or less connected trabeculae). After initial drop the further reduction of this parameter is less dramatic.
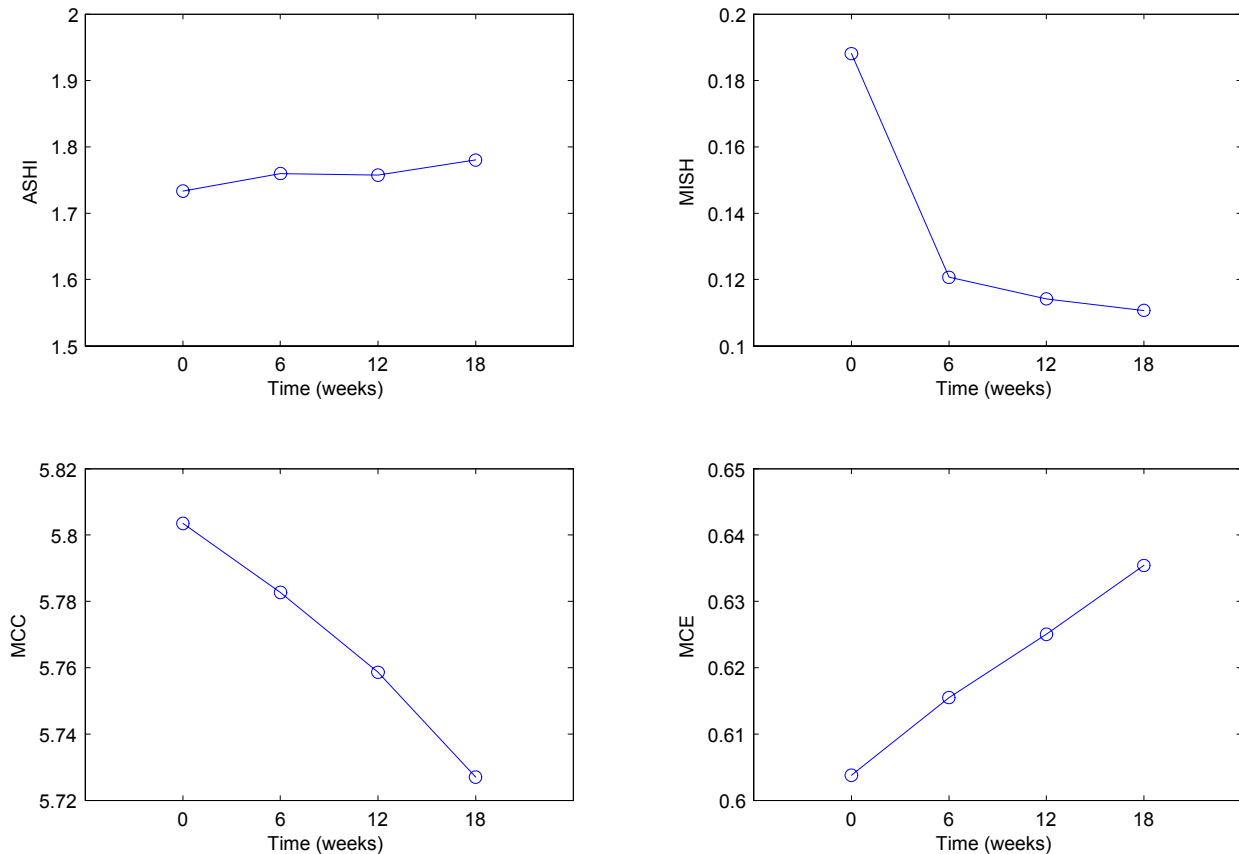
Figure 3.3. Shape-based structural measures of complexity during 18 weeks after band rupture trauma calculated from the trabecular bone VOI.

Both marching cubes based measures, the MCE and the MCC, reveal a decrease of the surface complexity. Both measures show a linear evolution over time.

The mean curvature H and the total curvature K were computed for the entire bone, because the current version of the corresponding Amira module does not allow the computation within a given VOI. However, the mean curvature H increases during the fixation of the patient, clearly indicating that the trabecular structural elements become thinner (Fig. 3.4). The total curvature K is negative, indicating more concave surfaces than convex surfaces, which is in contradiction to the findings based on ASHI. This may be an effect due to the usage of the entire bone VOI. Nevertheless, this value increases over time and, thus, confirms the findings of the Phase II of the Project, where we found an increase of K during bone loss in tibia.

The last two considered measures are the Moran's I index and the lacunarity. Both measures reveal an increase of the translational invariance within the trabecular bone after immobilization, i.e., different regions of the analyzed bone volume become more and more similar. This is also an indicator that the trabecular bone loses its complexity (Fig. 3.5).

In addition, the morphometric measures BV/TV, Tb.N, Tb.Th and Tb.Sp were calculated by the Scanco's CT-software, allowing us to compare and verify the results. The BV/TV measured by the CT-software shows exactly the same behavior as the BV/TV calculated by the developed Amira modules (Fig. 3.6). The smaller values of the BV/TV provided by the CT-software perhaps could be explained by the fact that the algorithm implemented there derives BV/TV from the BMD, while we use direct estimation of BV/TV from noise-reduced data. Smaller values for the derived morphometric parameters are also reported in the article Boutroy et al. 2005.
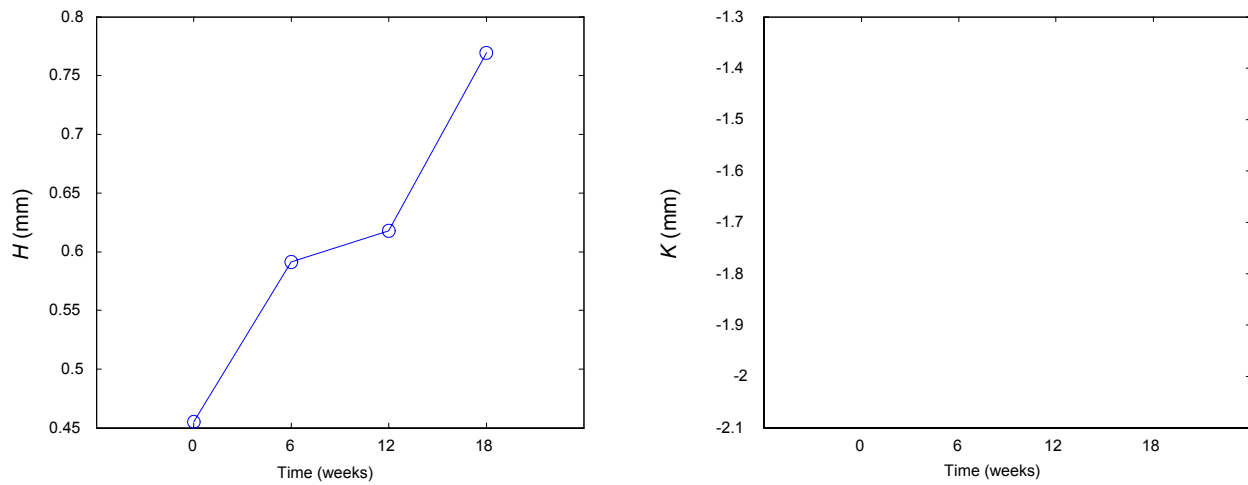
Figure 3.4. Mean *H* and total *K* curvatures for both trabecular and cortical bone surfaces after band rupture trauma.
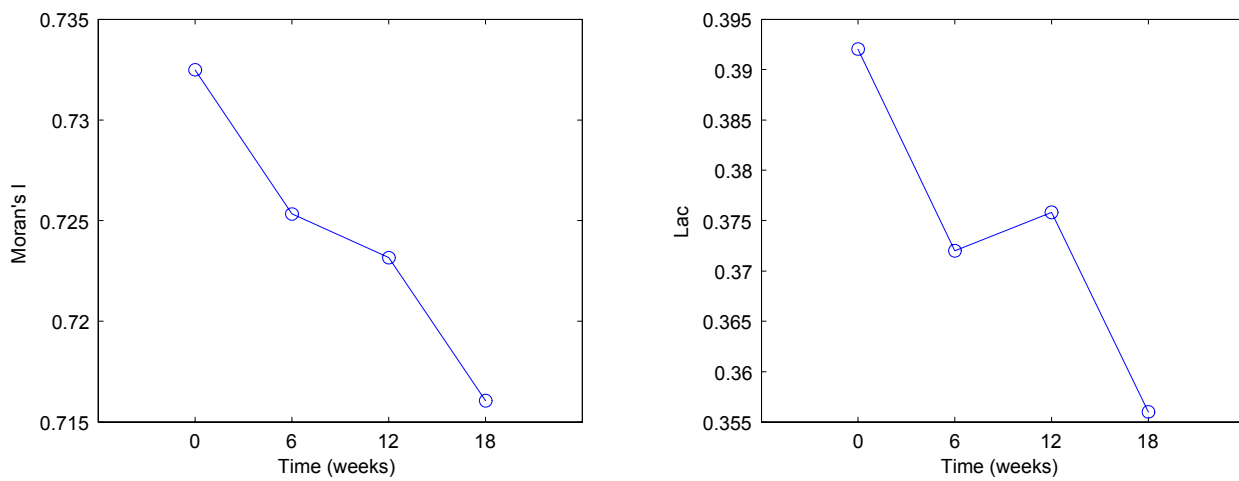

Figure 3.5. Moran's *I* index and Lacunarity *Lac* for trabecular bone surface during 18 weeks after band rupture
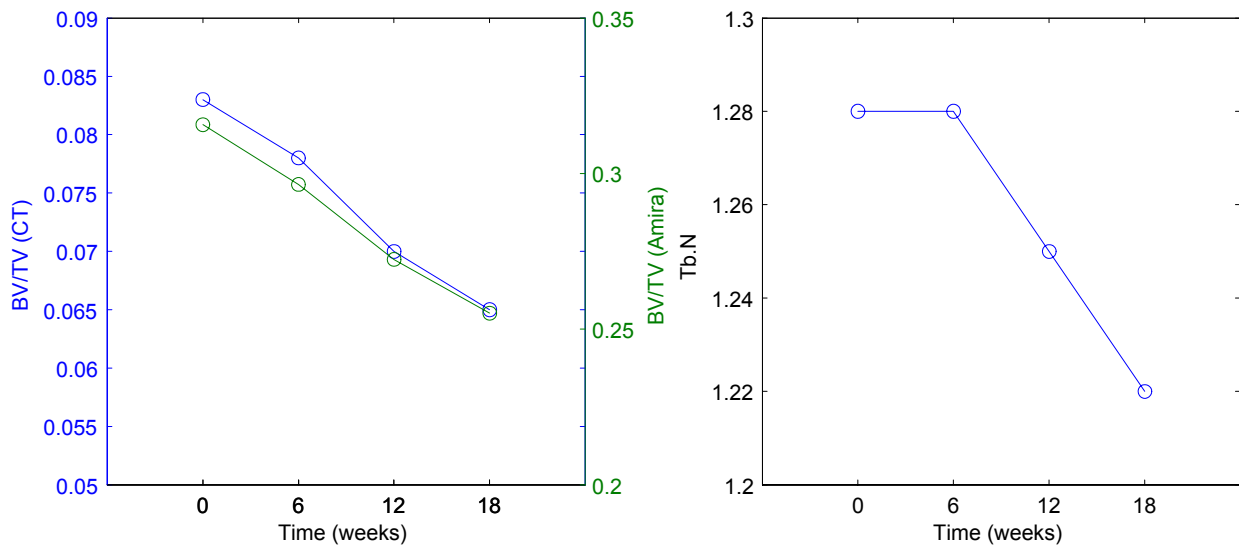

Figure 3.6. *Left:* bone volume fraction BV/TV (CT) provided by the 3D pQCT scanner software (*blue curve*) and the BV/TV (Amira) calculated by the developed approach (Final Report Phase II, 2006, *green curve*). *Right*: trabecular number Tb.N [1/mm] calculated by the scanner software.
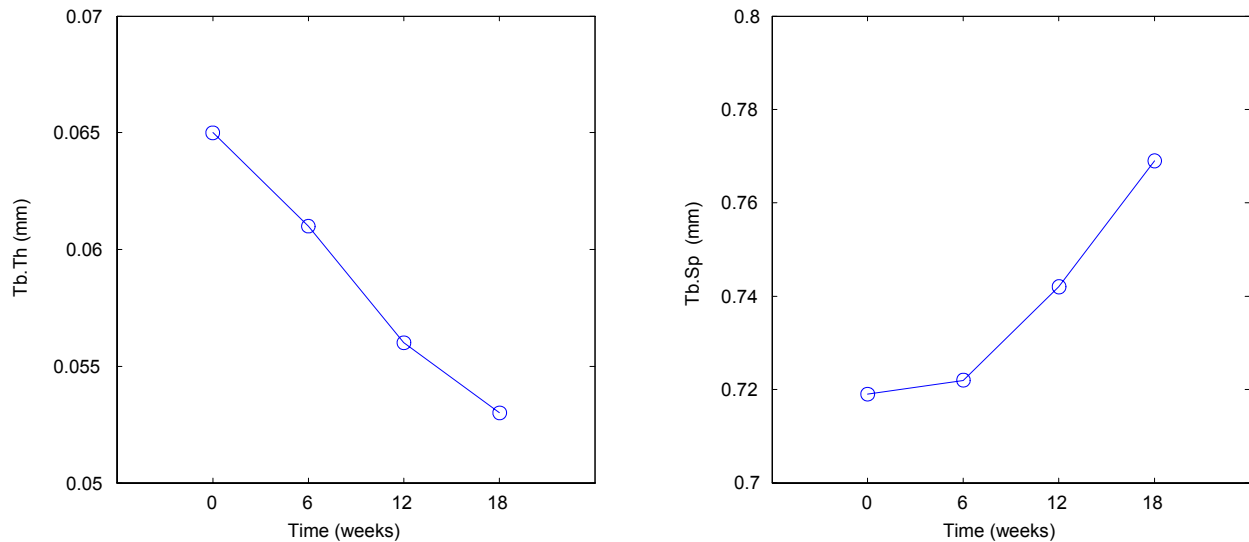
Figure 3.7. Trabecular thickness Tb.Th (*left*) and trabecular separation Tb.Sp (*right*) in distal tibia during 18 weeks after band rupture trauma.

The trabecular thickness Tb.Th decreases over time, and that confirms our findings based on the mean curvature (Fig. 3.7). The trabecular separation index Tb.Sp shows a minor change during the first six weeks, but it demonstrates a steep linear increase, indicating that the space between the trabecular elements becomes wider. This result is similar to that of the total curvature (Fig. 3.4), which is, however, more related to the concave and convex shapes of the trabeculae. In contrast, the measure MISH shows during the first six weeks a more dramatic change, and then a moderate change (Fig. 3.3). Therefore, we can infer that these measures really represent different features of the trabecular bone.

3.3 Experiments to Establish Minimal Required Resolution

For the tests of a minimal required resolution for the structural quantification of the trabecular microarchitecture we used the µCT scans of entire lumbar vertebra L3 with voxel size of 37 µm acquired by Scanco Medical AG during previous phase of the Project (Final Report Phase II, 2006). This is a work in progress. The results reported here are obtained from 11 specimens including normal, osteopenic, and osteoporotic bones with BV/TV in the range from 2 to 18.5 %.

In these computer experiments we modelled that the vertebral data were acquired with different resolutions which are lower than the resolution of the original data. We simulated the low resolution images by downsampling the present data sets using a Lanczos kernel (Final Report Phase I, 2003, Lehmann et al. 1999). Next, to compare the SMCs at different resolutions, we resampled the data back to the original voxel size. The VOI was selected similarly to the previous study (Final Report Phase II, 2006) as a vertical cuboid of size 10 mm × 10 mm × 25 mm located in the centre of the vertebra; the SMCs were calculated for the trabecular bone within this VOI.

We downsampled the µCT images to 10, 30, 50, 70 and 90% of the original geometrical size, corresponding to a reduced resolution, or larger voxel size, as summarized in Table 3.1.

Table 3.1. Downsampling and corresponding voxel size simulated in the experiments.

Downsampling (%)	10	30	50	70	90	100
Voxel size (µm)	370	123	74	53	41	37

For the simulated images with resolutions between 50 % and 90 % of the original resolution, the BV/TV, lacunarity and the SMCs based on symbol encoding do not change significantly. For lower resolutions, especially for the extremely low resolution of only 10%, these measures change dramatically (Fig. 3.8).

In contrast, curvature measures and shape-based SMCs are more sensitive regarding the resolution (Fig. 3.9). Whereas such SMCs as the ASHI, the SHC, and the MISH show a linear dependence on the voxel size, the mean and total curvatures H and K, the Moran's I index, as well as the MCE and the MCC show a more critical shift in their values resulting in changing the ordering of the samples (intersecting curves in Figure 3.10).

Nevertheless, all measures show a critical change for too low resolutions below 30% of the original resolution.
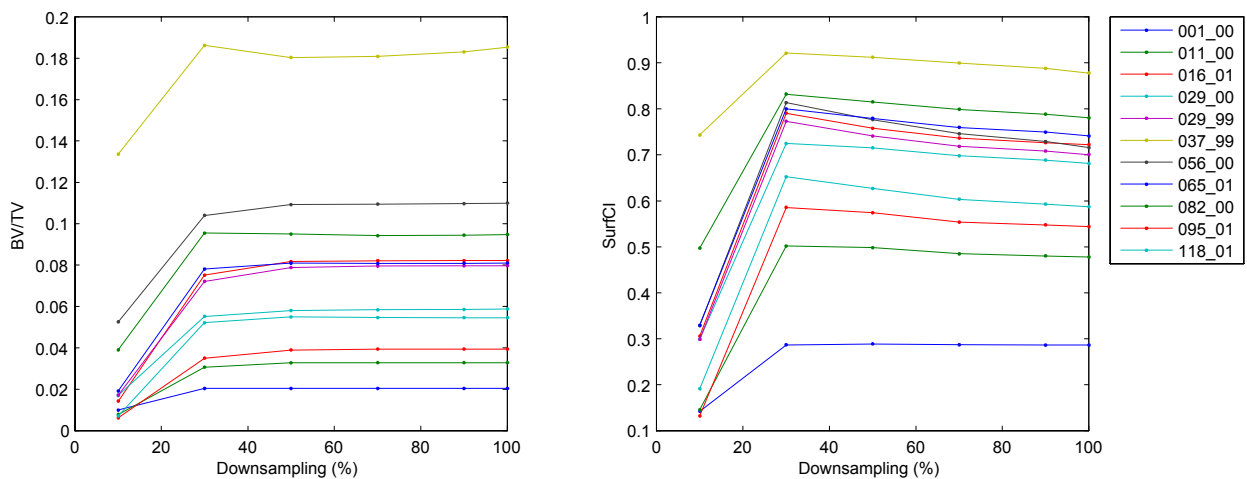

Figure 3.8. Dependence of bone volume fraction BV/TV (*left*) and one of the symbol-encoding based measure surface complexity index SurfCI (*right*) on different voxel size of the µCT images, simulated by downsampling. Curves of different colours represent different bone specimens whose IDs are shown in the table at the right. The other symbol-encoding SMCs and the lacunarity demonstrate similar behaviour.
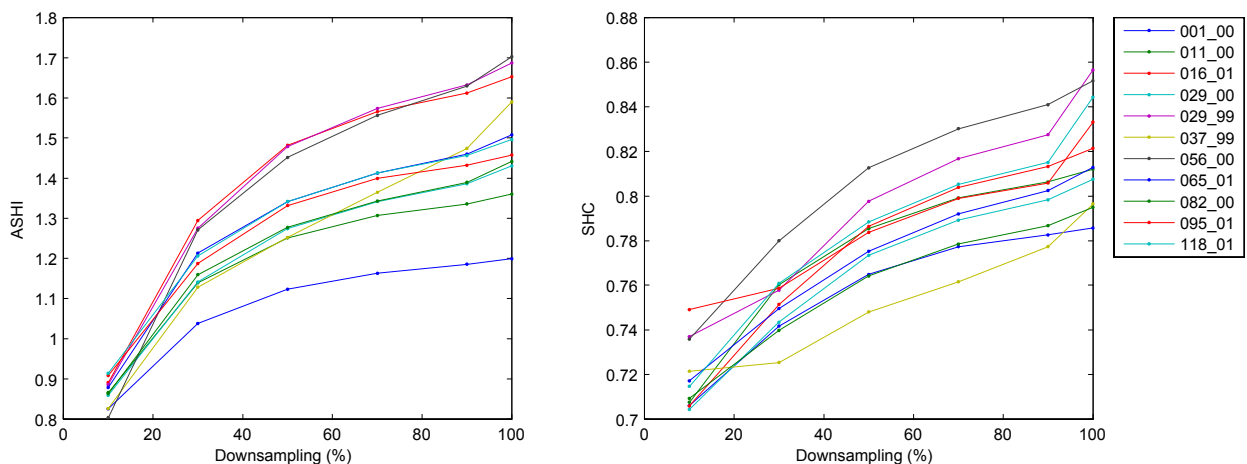

Figure 3.9. Shape-based SMCs the Averaged Shape Index ASHI (*left*) and the Shape Complexity SHC (*right*) for different voxel size of the µCT images simulated by downsampling.
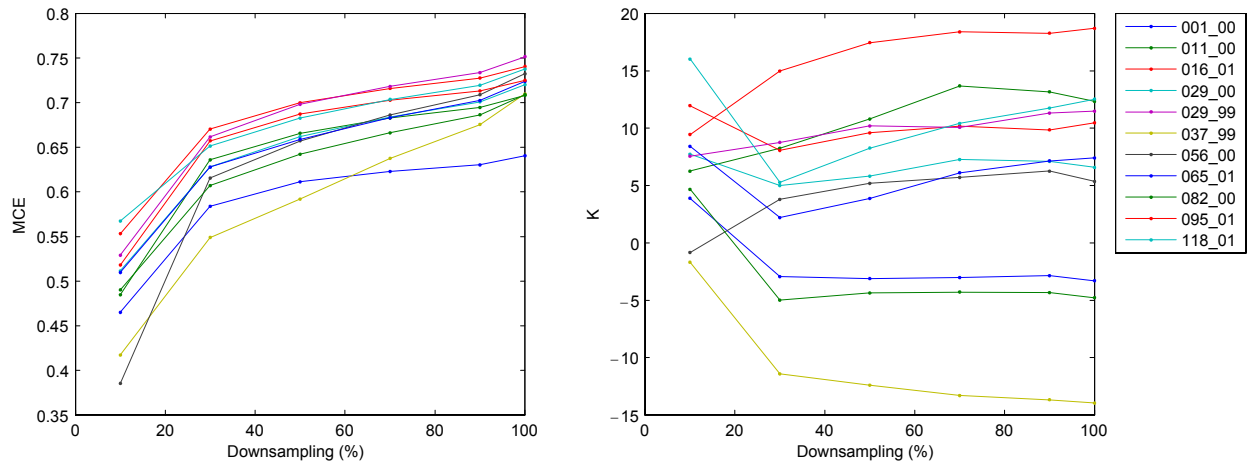
Figure 3.10. One of the marching cube based SMCs, the Marching Cube Entropy MCE (*left*) and total curvature *K* (1/mm, *right*) for different voxel size of the μCT images simulated by downsampling

Furthermore, the found sensitivities can differ for different samples. E.g., normal bone sample 037-99, which has a rather high bone density (calculated BV/TV is 18.5%, histomorphometric BV/TV is 13.6%), is much more sensitive on the resolution than the other samples. This may be a hint for different kind of microstructure in this sample, which heavily changes under resampling.

In order to estimate the influence of resolution on differences in structural measures during bone loss or between normal, osteopenic, and osteoporotic architectures, we selected the group of 11 specimens whose BV/TV covers the range from normal to osteoporotic and calculate the relation between the structural measures calculated from downsampled data and the BV/TV obtained by the histomorphometry (Final report Phase II, 2006). The results are summarized in Fig. 3.11.
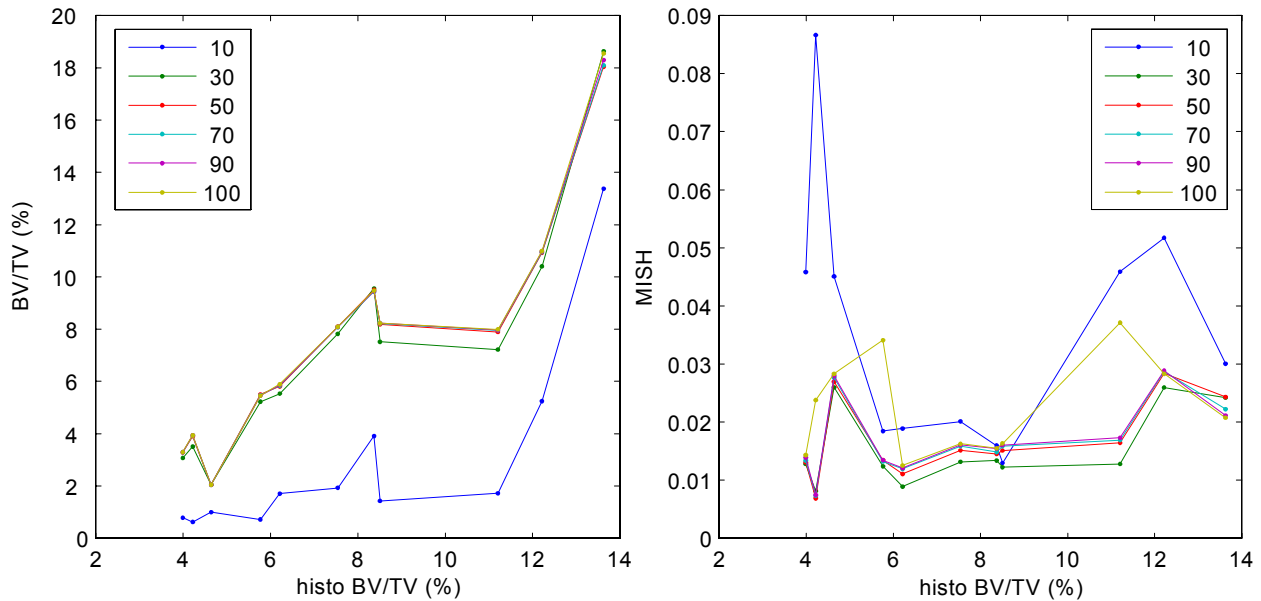
Figure 3.11. The bone volume fraction (BV/TV, *left*) and the Shape Mutual Information (MISH, *right*) estimated from the resampled images for group of 11 bone specimens compared with the corresponding BV/TV obtained by the histomorphometry. Each point of the curve represents the bone specimens. Curves of different colours correspond to the different resampling coefficient; its value in percent to the original data is shown in the inlays.

24

Next, in order to characterize quantitatively the differences in the SMCs induced by different voxel size, we have computed the Spearman's rank correlation between the SMCs of the original data of 11 specimens and the SMCs of the same set of specimens which µCT-data were resampled to the lower resolution or larger voxel size. Applying a threshold of 0.98 on the correlation coefficient, we estimated the minimal required resolution for the analysis of trabecular bone structure with the developed approaches (Table 3.2, Figure 3.12).

From this analysis we can infer the following preliminary statements:

1. The SMCs based on symbol encoding, BV/TV, as well as the lacunarity are not very sensitive on the resolution. These measures reveal valuable results also for images with voxel size larger than 100 µm.

2. The shape based measures and the mean and total curvatures are rather sensitive on the image resolution. For successful evaluation of the bone structure with these measures the voxel size of the µCT images should not be larger than 50 µm.

However, these findings are preliminary and this study is still in progress.

Table 3.2. Minimal resolution (in percent of the original µCT data resolution of 37 µm) required in order to get reliable results of bone structural evaluation.

BV/TV	SCI_{3D}	$SCI_{BV/TV}$	IGE	SurfCI	SurfIGE	S_n	H	K
30	30	30	30	50	30	50	70	90

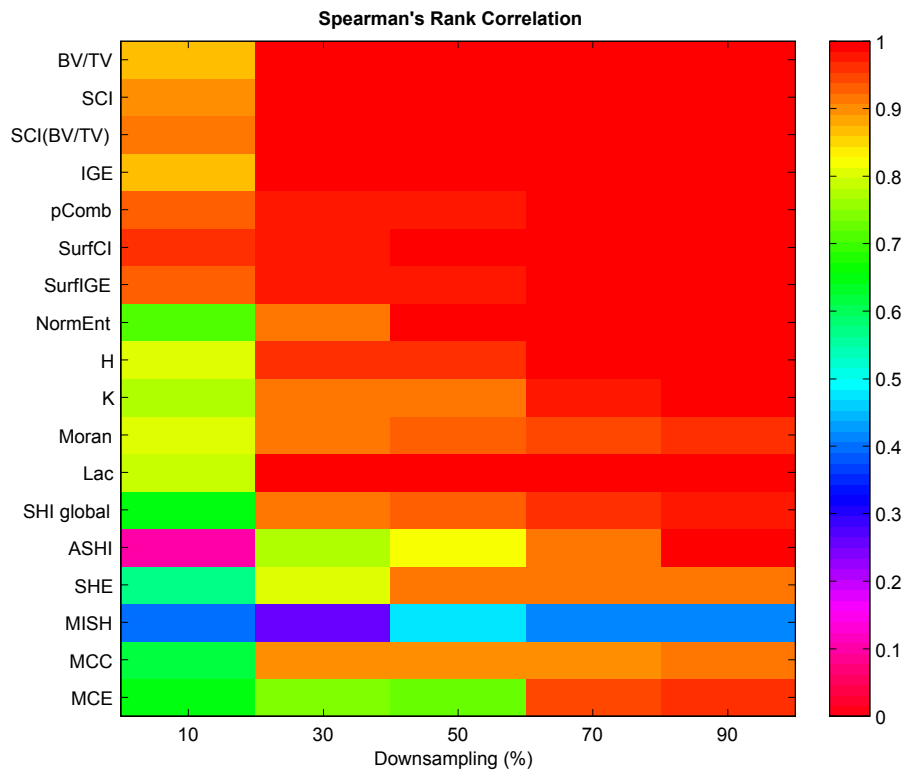| Moran Ind.	Lacunarity	SHI_{global}	ASHI	SHE	MISH	MCC	MCE
100	30	90	90	100	100	100	100

Figure 3.12. Spearman's rank correlation coefficients for the analysed SMCs within the group of 11 vertebral specimens and for different resolutions. Different colours represent different values of the correlation coefficient as shown in the colour scale at the right.

4. Developing New Types of Measures Based Primarily on Mechanical Considerations, and Testing their Predictive Power against the Experiments

4.1 Development of Mean-Field Approach Based on Mechanical Assessment of Nodes in a Cellular Structure in Order to Evaluate Trabecular Bone Architecture

In order to predict the mechanical behaviour of trabecular bone, the standard approach is to correlate a morphological parameter, such as trabecular thickness or spacing, with mechanical properties obtained from real or virtual mechanical tests. Although many parameters can be found to correlate, an understanding of the mechanical basis of why a given parameter correlates is often missing. Our approach to this problem is to choose morphological parameters for which we know the mechanical consequences, at least on a local level. For this we simplify the network-like trabecular architecture into a set of connected joints or "nodes", where a node is defined by the trabeculae which meet each other in a junction point (Fig. 4.1, top). A node geometry that favours deformation by bending is mechanically unfavourable. Such "weak" nodes could initiate bone fracture and should be therefore identified in an image of trabecular bone.

The problem was tackled in two steps. Firstly, a clear definition of a "weak" node had to be given. This was done by investigating the mechanical behaviour of a periodic lattice constructed of nodes of a single geometry (Fig. 4.1, left). The stiffness matrix can be calculated analytically, and gives the elastic response as a function of node geometry. Secondly, the mechanical response of a node in a regular, isotropic lattice (Fig. 4.1, right) was investigated numerically using commercial finite element software. These investigations were started with a two-dimensional cellular solid with a simple geometry, where the nodes have a coordination number of three.

The model was tested for a multitude of different node geometries, both for uniaxial and biaxial loading. Figure 4.2 (left) illustrates the distribution of strain energy density around a mechanically weak node within a regular lattice under vertical uniaxial loading. The maximum of the anisotropic, long-ranged pattern of the strain energy is not at the location of the inserted
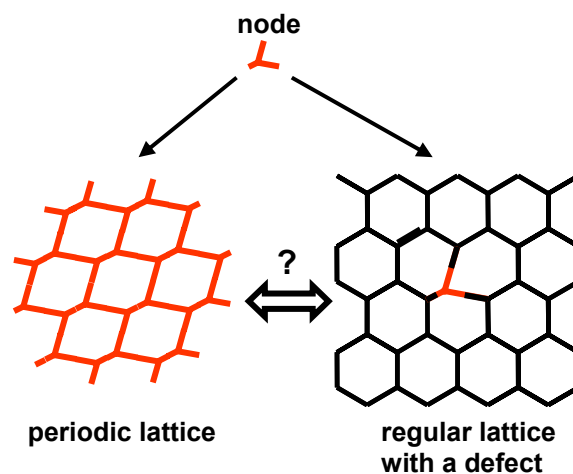

Figure 4.1. Mechanical assessment of a node, being either part of a periodic lattice (*left*) or implemented as a defect in a regular lattice (*right*). Since the periodic lattice is theoretically much easier to handle, an important question is how much of the information gained from periodic lattices can be used to predict the response of a node acting as a defect in the regular lattice.
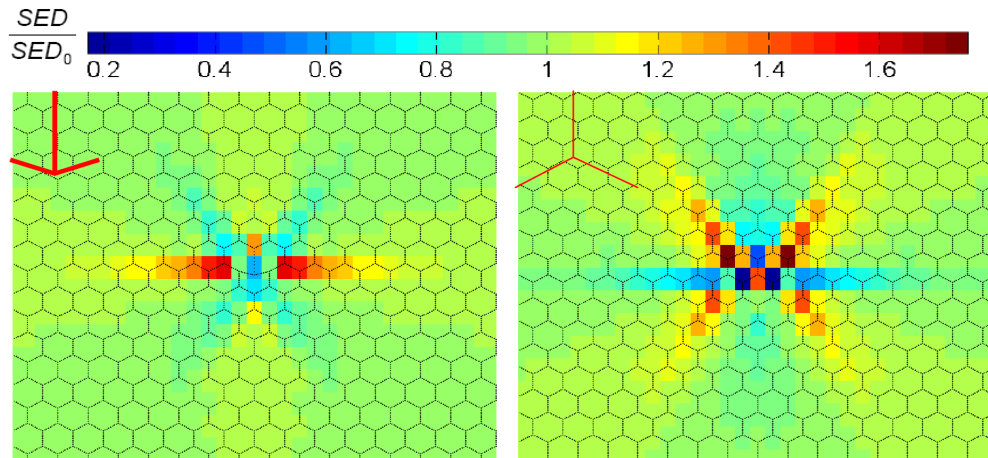
Figure 4.2. Strain energy density (SED) of the regular lattice with defect after vertical compression. The red nodes on the upper left corner represents the type of defect introduced in the middle of the regular lattice: a geometrically weak node (*left*) and a node with reduced thickness (*right*).

defect, but at its second nearest neighbour. Another example of a strain energy concentration away from the defect can be observed when a regular node, but with a reduced thickness is introduced into the lattice (Fig. 4.2, right). In this case the strain energy density has its maximum values at the third nearest neighbours of the defect.

These investigations showed that the introduction of weak elements in a cellular structure leads to an increase in the overall strain energy. Interestingly this strain energy is not necessarily concentrated at the weak node, but rather in its neighbouring environment. This has important consequences on the mechanics of trabecular bone, in that elastically weak portions of the structure may not fail themselves but rather cause failure in their neighbouring environments.

4.2 Development of a Lattice-Dynamics Based Approach to Predicting Deformation Localisation in Cellular Solids

Cellular solids, including trabecular bone, tend to fail through the localisation of deformation within a plane, which has a defined orientation with respect to the architecture and applied load. We are interested in investigating the effect of the underlying architecture on the localisation of deformation in trabecular bone (Nazarian and Müller 2004). Our first efforts have focused on more idealised, periodic cellular solids made up of networks of beams. These systems are computationally more tractable than trabecular bone, and have the added advantage that their periodicity enables us to apply analytical tools developed in the solid state physics community.

The model is inspired from the work of Born, Huang (1954) and Khachaturyan (1983) the mechanical instabilities of metallic crystals. This approach consists firstly of determining the effective elastic potential of a beam between two joints as a function of its orientation and a homogeneously applied strain. The potential gives the local change in elastic energy of the beam (increase or decrease) due to perturbations in the beam joints, a decrease in energy indicating that a given perturbation is energetically favourable and likely. The second step uses the underlying architecture to calculate the energy of the entire lattice of beams as a function of all the local perturbations of the joints in the lattice. This gives an equation of $d \times N$ variables where d is the number of degrees of freedom, and N is the number of joints in the lattice. Such an equation can be reduced to d variables by using the fact that any perturbation can be written as the sum of perturbation waves, meaning we simply look at the lattice in reciprocal space. The change in

elastic energy can then be investigated as a function of deformation mode and direction. Deformation localisation will occur when the elastic energy becomes negative in a given direction (and applied load).

The classical lattice dynamics approach of Born-Huang has been successfully applied to beam lattices in two dimensions, and allows the prediction of the low-energy deformation directions in simple systems as a function of the external deformation field. For example, Figures 4.3 and 4.4 show the energy of deformation localisation in a two dimensional square lattice as a function of the wave vector for different applied strains. After a certain critical strain in the x-direction, deformation localisation becomes energetically favourable in the y-direction (Fig. 4.4). This can be seen more clearly in Figure 4.5 which illustrates the energy of a deformation localisation within a plane as a function of the localisation angle with respect to the 10 direction. The different curves illustrate the effect of changing the orientation of the external deformation field on the elastic energy of localisation.
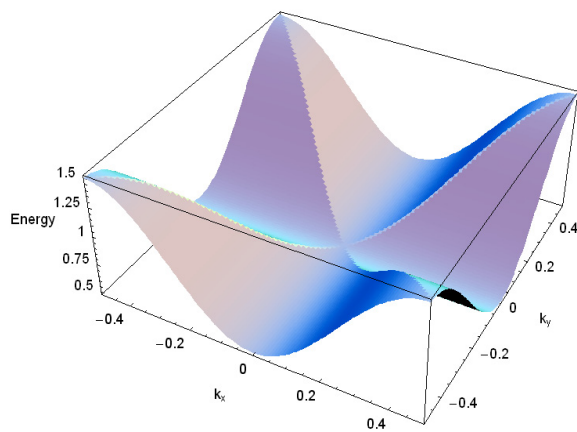

Figure 4.3. Energy surface as a function of wave vector for a square lattice at zero applied strain.
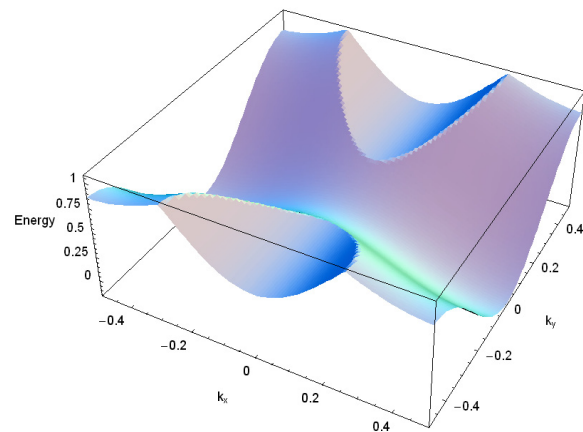
Figure 4.4. Energy surface as a function of wave vector for a square lattice at an applied strain in the x direction of -0.3.
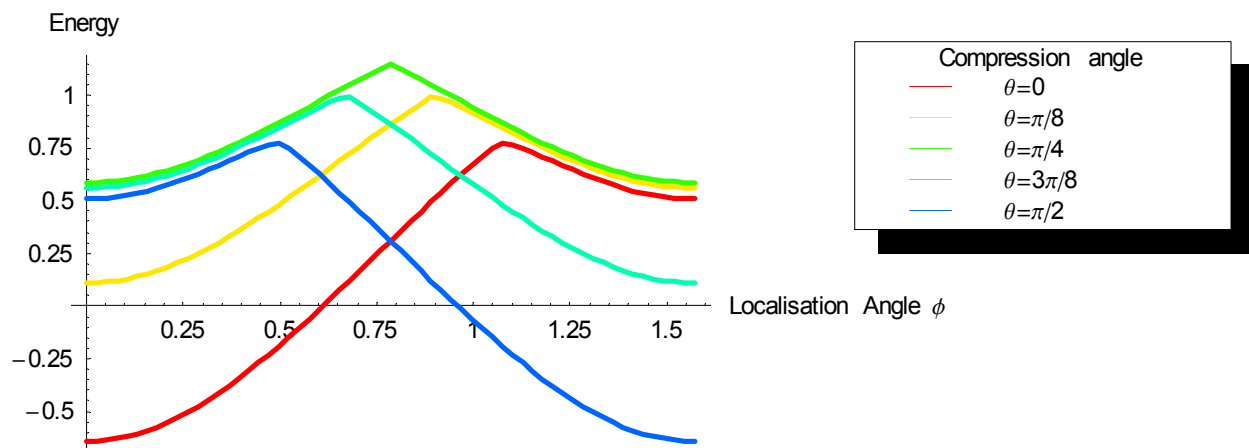

Figure 4.5. The energy of deformation localisation within a plane under uniaxial compression as a function of the localisation direction ϕ and orientation θ of the applied compressive strain of -0.3.

5. Computer Simulations of Bone Remodelling with Increased Turnover Using Different Implementation of Feedback Mechanism Based on Wolff-Roux Law. Characterization of the Dynamical Changes in Bone Architecture

The architecture of trabecular bone derives from the process of remodelling in which osteoblasts and osteoclasts add or remove bone respectively. These cells are thought to be mechanosensitive which has the consequence that bone is deposited where it is mechanically needed and removed otherwise, giving rise to the so-called "Wolff-Roux law". The modifications of architecture from cell action in turn changes the local mechanical stimulus giving rise to a feedback effect between architecture and cell response. We have investigated the influence of cell response to mechanical stimulus on the bone remodelling process using three dimensional computer simulations.

The simulations are based on the cellular automata approach, in which the trabecular architecture is mapped to a cubic lattice, with bone and marrow being represented by occupied and empty sites on the lattice respectively (see Fig. 5.1 for outline of model). At a given time in the simulation the local stress/strain distribution within the trabecular structure is calculated, which in turn gives the stimulus for osteoblast or osteoclast action. The probability for addition or removal of a bone "packet" as a function of this stimulus is given by a remodelling rule (Fig. 5.2) which can be modified to simulate the action of drugs or disease on cell action. The deposition or resorption site is determined stochastically, the new architecture is calculated and the process is repeated iteratively. A fast algorithm for the mechanical calculation is used which enables large lattices to be studied (256^3 voxels) for long simulation times (>100 years of bone remodelling).
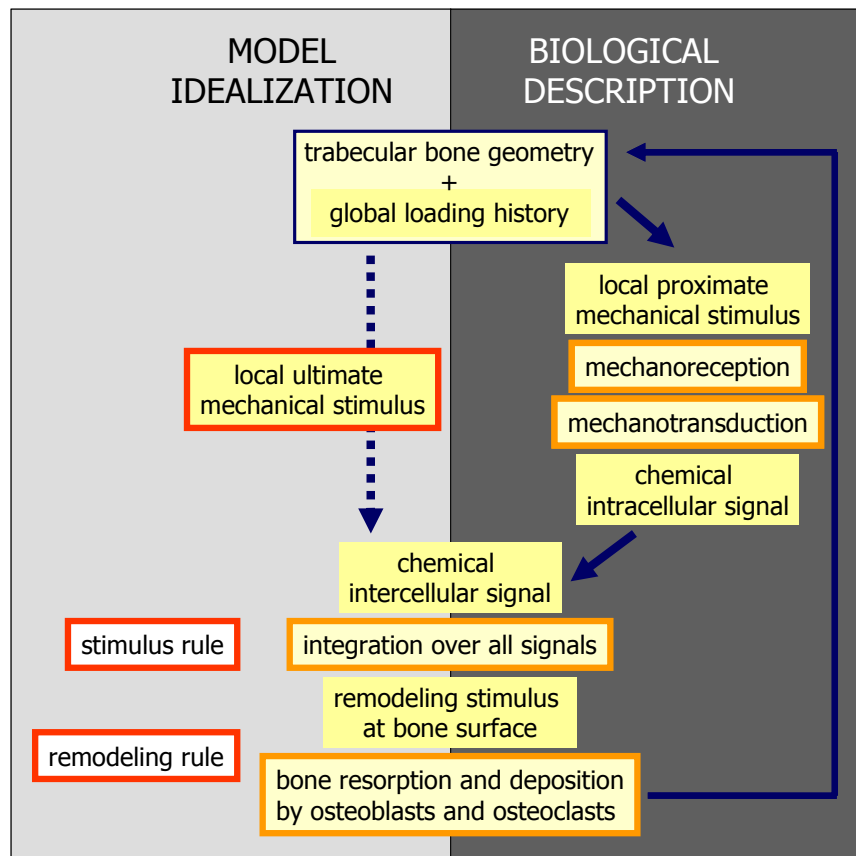

Figure 5.1. Flow chart of the bone remodelling process: complete biological description and model idealization.
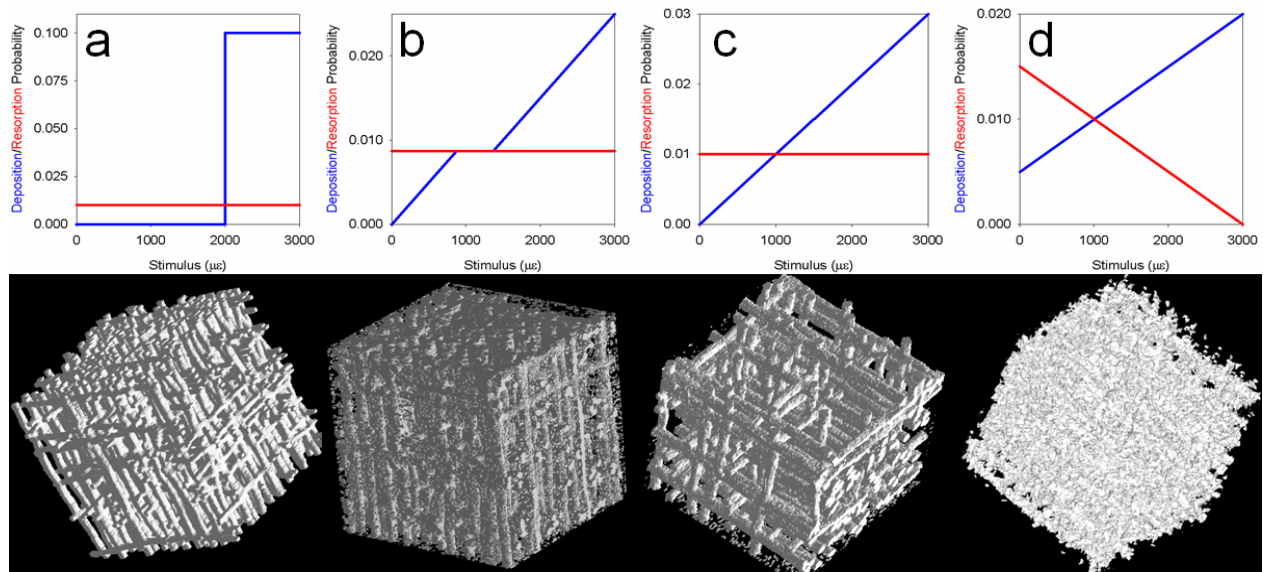
Figure 5.2. Snapshots (*low row*) of the remodelling process after 30 years of simulation time for different sets of corresponding "remodelling rules" (*upper row*).

Figure 5.2 illustrates the snapshots of different simulations for different remodelling rules after 30 years of simulated bone remodelling. It is clear that the remodelling rule has a strong influence on the type of trabecular architecture that is produced. The rules (a) and (c) giving rise to much smoother trabeculae than (b) and (d). Often in the literature remodelling has been simulated by net-remodelling rules that are the sum of osteoblast (positive) and osteoclast (negative) action as a function of mechanical stimulus. This was tested using the simulations illustrated in Figs. 5.2, (c) and (d), which were chosen to have the same net remodelling rule, but with different osteoclast and osteoblast remodelling rules. The results clearly show large differences in trabecular architecture and highlight the necessity of separating the two processes of deposition and resorption. Concerning bone mass all systems simulated reached homeostasis, however remodelling continues and the underlying architecture continues to evolve. Trabeculae are continually being lost during remodelling which result in a coarsening of the remaining trabeculae. Typical coarsening velocities (trabecular area increase per year) are on the order of 10^{-4} mm^2 year^{-1} which is well in agreement with the experimental data of Stauber and Müller (2006) in which a coarsening velocity of $\sim 5 \times 10^{-5}$ mm^2 year^{-1} was measured in human trabecular bone. The influence of changing osteoclast activity (related to therapeutic treatments) and external load (exercise) were also investigated and result in very different responses for the different remodelling rules. This highlights the importance of quantifying the exact nature of the response of cells to external stimuli in order to design better treatments against bone disease.

30

6. Developing 3D Image Processing and Visualization Tools for Quantitative Analysis of Changes in Micro-Architecture

6.1 3D Image Processing to Prepare Data for Rapid Prototyping

A rapid prototyping pipeline was developed in Amira that supports as input either 3D voxel data like 3D μCT images or surface models like the 3D CAD files and stores the result in the format readable by rapid prototyping system including suitable processing instructions (see Figure 6.1). The processing pipeline is available as an Amira module. The user can select a sub-volume of the input and processing parameters, such as the threshold separating bone from background in the image data. Based on the chosen parameters, the rapid prototyping module automatically performs the necessary calculation and transformation, and prepares voxel data that are suitable for the Envisiontec Perfactory RP-machines. The last step is to export the data in a file format supported by the rapid prototyping system. The module can be adjusted to meet the requirements of other RP-systems.
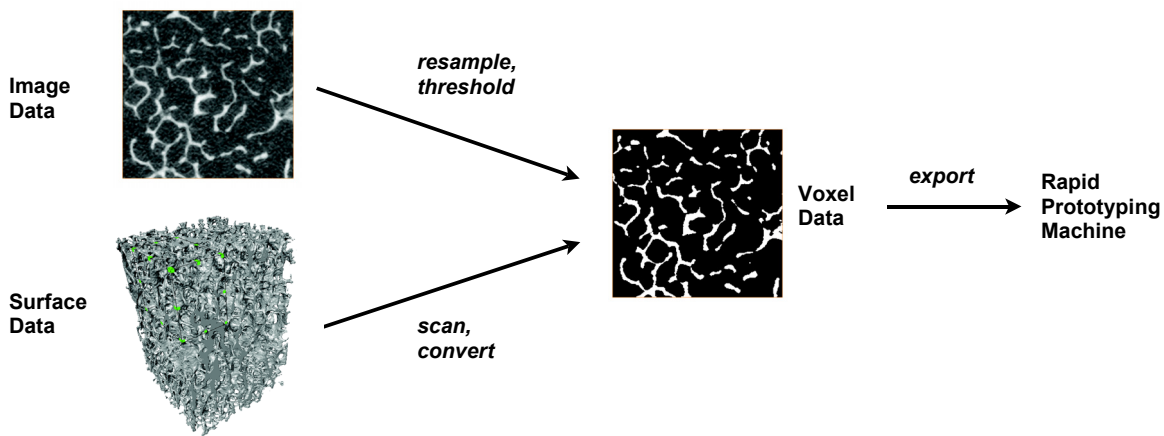

Figure 6.1. Rapid prototyping workflow: the input can either be image data or a surface model. An Amira module computes voxel data suitable for export to the rapid prototyping machine according to user specified parameters.

6.2 Architectural Decomposition of 3D Trabecular Bone Structure

A method was established that is able to decompose data computed by a bone remodeling simulation (see Final Report, Phase II, 2006 and Sect. 5 of this Report) into its architectural elements and establish a correspondence of such elements between each two steps of the simulation. This is the first step towards tracking of architectural elements through a complete 3D data series and the consecutive application of the acquired information for visualization and possible assessment architectural changes.

The approach we develop combines various 3D image processing methods (see Figure 6.2). The processing sequence can be outlined as follows: Input data from a 3D bone remodeling simulation are filtered to yield a smooth voxel objects. Thinning procedure computes a voxel skeleton, which is next cut at the branching points. A watershed transformation propagates the labeled edges of the voxel skeleton to fill the whole structure. The resulting volume elements are tracked between two consecutive simulation steps by computing volume overlaps between the architectural elements.

Input data from the bone remodeling simulation exhibit noisy voxel surfaces and, therefore, need to be smoothed in order to create a smooth voxel object. This is needed because thinning is too
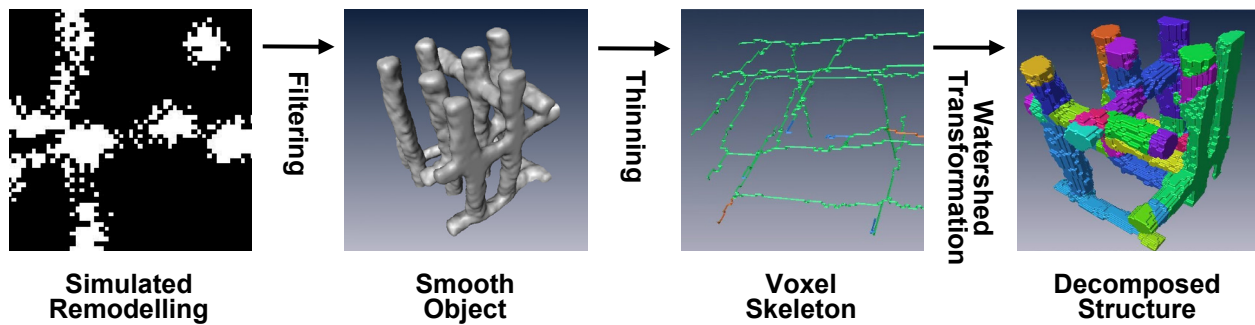
Simulated Remodelling → Filtering → **Smooth Object** → Thinning → **Voxel Skeleton** → Watershed Transformation → **Decomposed Structure**

Figure 6.2. Decomposing architecture: Output data of simulated bone remodeling needs to be smoothened. Thinning procedure computes a voxel skeleton that is cut at the branching points. A watershed transformation fills the volume resulting in the decomposed structure.

sensible to small topological changes resulting from noise, like tiny loops on the object surface. Such loops must be avoided. Experiments were conducted to determine suitable filtering parameters and revealed that Gaussian smoothing provides a sufficiently smooth voxel object while retaining the architecture of the structure.

The next step is to apply topological thinning to the smoothed voxel object. After the voxel object is converted to a grid cell representation, which explicitly contains the vertices, edges, and faces of voxels, grid cell thinning (Prohaska, 2007) computes a one-dimensional voxel skeleton. Lines with end-points not connected to loops are retained if they are geometrically important. The algorithm requires a parameter that quantifies the length of voxel paths to be retained. Experiments were conducted and it was decided that the length of six voxels is the best compromise between side branches retained and robustness to noise.

The grid cell representation makes it easy to decompose the voxel skeleton into elements. The number of directly neighboring line segments determines if a zero-dimensional cell is a branching point. Branching points are removed from the voxel skeleton. A connected component labeling assigns different labels to each line segment. A watershed transformation (Roerdink & Meijster, 2000) propagates these labels to fill the complete volume resulting in the architecture decomposed into volume elements.

Corresponding elements in two analyzed data sets are matched by computing volume overlaps. A matrix containing overlap between all elements in the first and all elements in the second data set is the base of the analysis. For each row of the matrix the column with the highest overlap is identified. If the overlap is clearly larger than the second largest overlap the elements associated with the row and column are identified as a pair of corresponding elements. All other cases are currently marked as 'unclear'. Further work is needed to handle unclear cases during tracking.

Based on the established architectural decomposition, two main tasks will be tackled in the second half of the project. The first task is to establish a method to track architectural elements through series of data sets and visualize architectural changes detected. The second task is to visualize relations between structural measure and architecture.

7. Ultrasonic Assessment of Bone Structure in Proximal and Distal Tibiae

During the reported period the ultrasound team concentrated its efforts on the following tasks:

- To extend the method of ultrasonic measurements in proximal tibia developed during the previous phase of the Project (Final Report Phase II, 2006, Tatarinov et al. 2005) onto the distal tibia with necessary modifications and adjustments;
- To broaden ultrasonic testing modalities potentially applicable for assessment of changes in the trabecular bone structure in the proximal and distal parts of human tibiae, and to develop corresponding experimental ultrasonic instrumentation;
- To evaluate with the developed ultrasound approach new tibial bone specimens obtained by project partners (see Section 1).

7.1 Methods and Technique

The study included continued search for appropriate ultrasonic modalities capable to assess structural changes in the trabecular tissue of the human tibiae applying unilateral access through a thin cortex. The following considerations were taken into account: In human tibia, zones of relatively uniform acoustic properties subordinated to bone structure, as it was found earlier using the surface transmission, are orientated transversally to the bone axis in the margin proximal and distal parts of the bone (Yanson et al. 1984), i.e. in the anatomical sites that correspond to the current locations of interest (Fig. 7.1). This condition suppo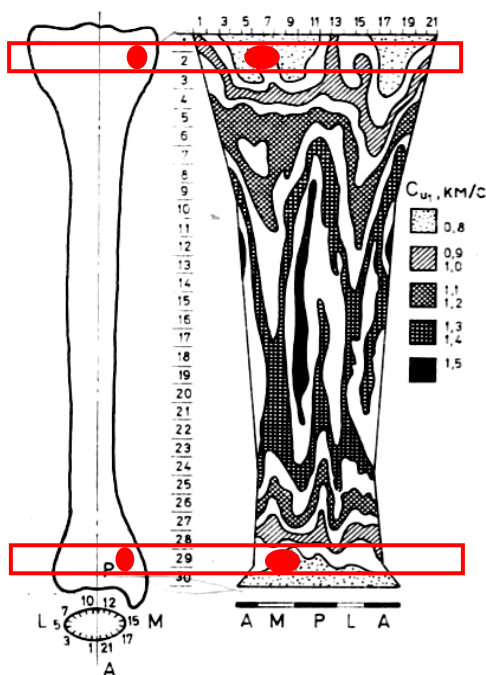ses transversal orientation of the acoustical base in order to follow the surface propagation of ultrasound being within approximately equal layer of the cortical thickness at certain levels of bone lengths and the similar bone structure. Thus, gradual changes of propagated ultrasonic signals can be assessed by linear profiling upon the bone surface in transversal direction. To provide propagation of subsurface longitudinal waves (so called lateral waves) and surface Rayleigh waves capturing possibly deeply into trabecular bone, the wavelength was increased by lowering ultrasonic frequency to 85-100 kHz. The second opportunity not exploited yet in such studies is ultrasonic backscattering. Advantage of this method is that the measurements can be produced at a single contact point on the bone surface. To overcome mismatch between possibilities of obtaining ultrasonic responses from trabecular bone through the cortex and traditionally applied high-frequency pulse-echo signals of several megahertz, an attempt to lower frequencies towards kilohertz range was undertaken. So two modalities were chosen for this study: 1) surface profiling, i.e. acquisition of propagated signals during gradually increasing acoustical base at the surface transmission; 2) pulse-echo measurements containing possible backscattering response from the trabecular structure in the rear (back) parts of echo signals (Fig. 7.2).
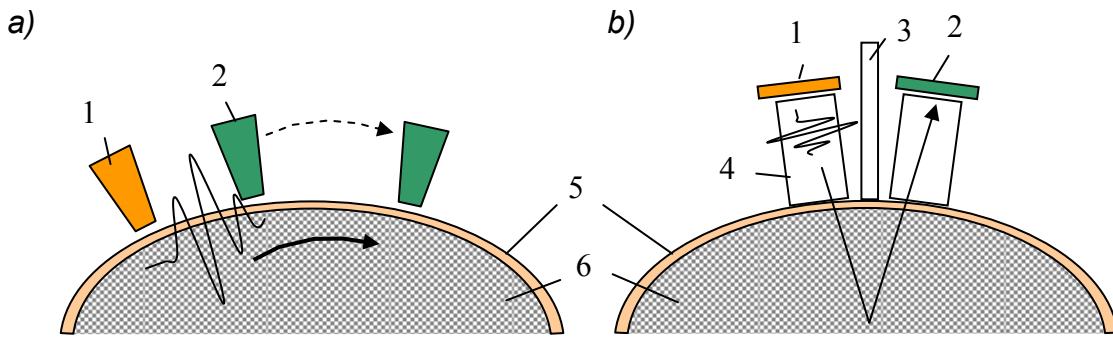

Figure 7.1. Zones of ultrasound velocity distribution in human tibia (Yanson et al., 1984) projected onto current regions of interest in proximal and distal tibiae (*marked with red*).

Figure 7.2. Schematic illustration of ultrasonic testing modalities: (*a*) – surface profiling by expanding acoustic base; (*b*) – pulse-echo measurements using dual-element transducer: *1*- emitting transducer; *2*- receiving transducer; *3*- acoustic isolation; *4*-acoustic prism; *5*- cortical bone layer; *6*- trabecular bone.

Custom-made experimental ultrasonic transducers were produced for each testing modality (Fig. 7.3). Two variants of surface transducers were manufactured with the lowest harmonics produced by the flexural resonances. Pulse-echo transducers for backscattering were realized as dual-element transducers with acoustic prisms forming pseudo-focusing within an object at 7–8 mm depth. Parameters of ultrasonic bone testing are given in Table 7.1.

Table 7.1. Experimental parameters for the ultrasonic examination of trabecular bone structure in proximal and distal tibia.

| Testing parameter	Surface transmission	Pulse-echo
Method of Bone Examination	Surface propagation. Profiling	Reflection
Applied Frequencies	85, 100, 150, 300 kHz	300, 600 kHz
Excitation Waveform	Gauss-enveloped sine,1 period	Gauss-enveloped sine, 3 periods
Acoustic Bases	Proximal tibia: 20-40 mm, step 5 mm Distal tibia: 12-20 mm, step 2 mm	Not applicable
Number of Repeated Measurements at each Location	3	6
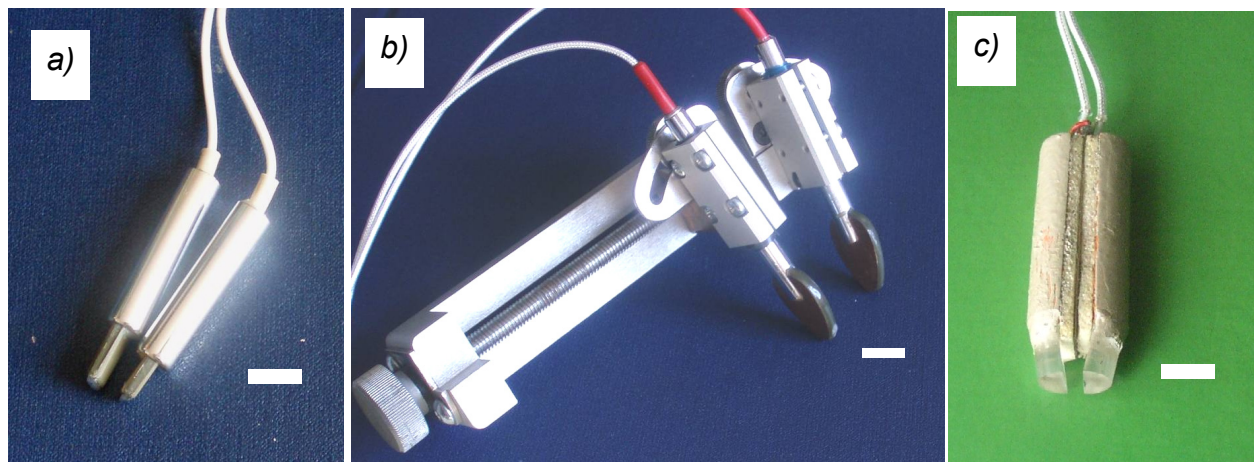
Figure 7.3. Custom-made ultrasnic transducers for surface transmission (*a, b*) and pulse-echo (*c*) modes: (*a*)- with rectangular piezoelements having resonances at 100 and 300 kHz; (*b*)- with drop-shaped piezoelememts, broadband with several peaks in 80–200 kHz range; (*c*)- dual-element with acoustical prisms. Whitre strips show linear scale length of 1 cm.

34

Prior to bone specimens testing, workability of the transducers was tested in phantoms mimicking changes of the material stiffness, porosity and amount of ultrasound scatterers dispersed in the medium.

7.2 Materials

To the moment, six human tibia specimens obtained from the partner CBF (see Sect. 1) were examined. The bones were recruited from cadaver donors of age in 73–88 year old range (73, 82, 84, 85, 87, and 88 years old). The specimens were intact isolated tibia bones sealed in plastic bags and preserved in NaCl solution in fresh condition. The specimens were kept at 4°C and examined at room temperature. The measurements were produced by pressing ultrasonic transducers to the bone surface through the plastic bag using water coupling media between the transducers and the bag for better ultrasound conductivity. The measurements in surface trans-mission and reflection modes were produced accordingly to the schemes shown in Figure 7.2, using three types of transducers (Fig. 7.3) and testing parameters as specified in Tab. 7.1. The measu-rements were performed in the middle of the medial surface of the tibiae, at the following levels: 17 mm below joint for proximal tibia and 13 mm above the ankle center (convexity peak) for distal tibia. Positioning of the transducers is shown in Figure 7.4.
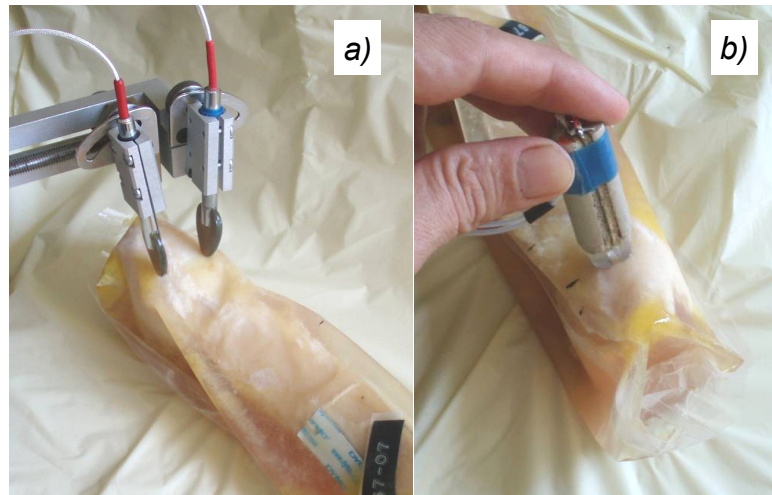

Figure 7.4. Positioning of ultrasonic transducers in distal tibia in surface transmission (*a*) and reflection (*b*) tests.

7.3 Preliminary Results and Collected Measurements Data

Currently, the acquired experimental data are in the processing. About 140 different ultrasonic signals were collected from one bone, the number being composed of measurements in distal and proximal parts, two modes of ultrasonic tests, several steps of profiling, and parallel repetitions. Total number of acquired and stored signals is close to one thousand. Necessity to create specialized software for data processing was revealed. The newly developed software will manage the initial ultrasonic signals, convert them to forms suitable for extraction of informative parameters, include averaging parallel records, noise filtering, frequency filtering, enveloping, presentation of surface profiling in 2D domain as function of propagation distance and spatial filtering, selection of informative regions of the signal matrixes and parameters calculation. The purpose of signal processing in the surface transmission is to determine velocities of fast and slow propagating wave packets, as well as attenuation of entire signals and their specific parts, obtained at different frequencies. In reflection mode, the signal processing is aimed to identify the region in echo-signals responsible on the backscattering from inner bone structures and to extract it from possible direct propagation and first reflections. Some typical signals obtained in the youngest and oldest available bones are discussed below as an illustrative comparison.

At first we considered primarily processed pulse-echo signals, in which rear portions can reflect changes of the backscattering from deeper lying bone structures. We have found that in the tibia of the older donor the rear area in the pulse-echo curve was smaller than for the specimen of a

younger donor (Fig. 7.5). This confirms the assumption that older bones have a rarefied trabecular structure which produces fewer reflections.

Next we considered the propagation signals in distal tibia of the same donors as above. The signals were obtained at 100 kHz main frequency and at acoustic base of 20 mm. In the older bone, a highly attenuated signal and a delayed propagation of the surface wave were found, see Figure 7.6.

Correlations between ultrasonic and structural parameters are expected after getting data from other partners and completion of ultrasonic data processing.
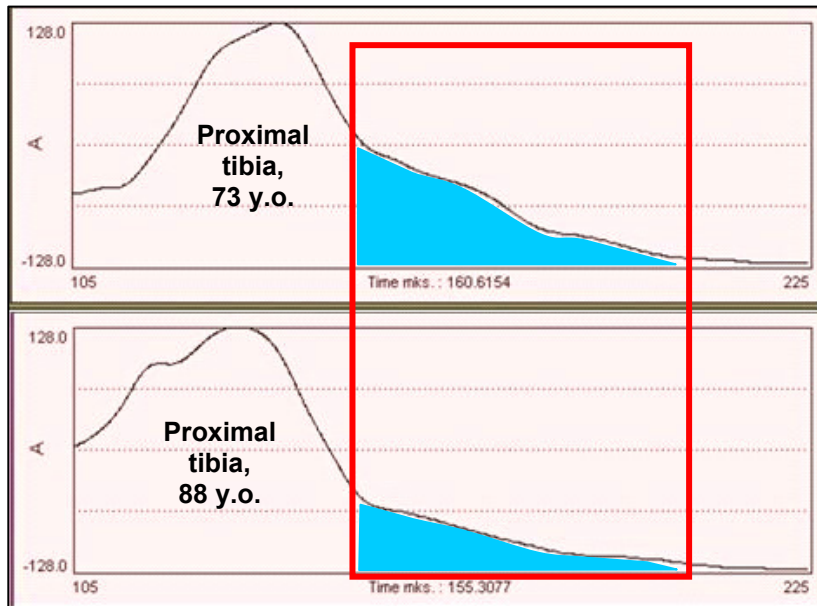
Figure 7.5. Enveloped and normalized pulse-echo signals in proximal tibiae of 73 and 88 year old donors. Marked by red area in selected rear portions of the signals reflect differences in backscattering from deeper structures.
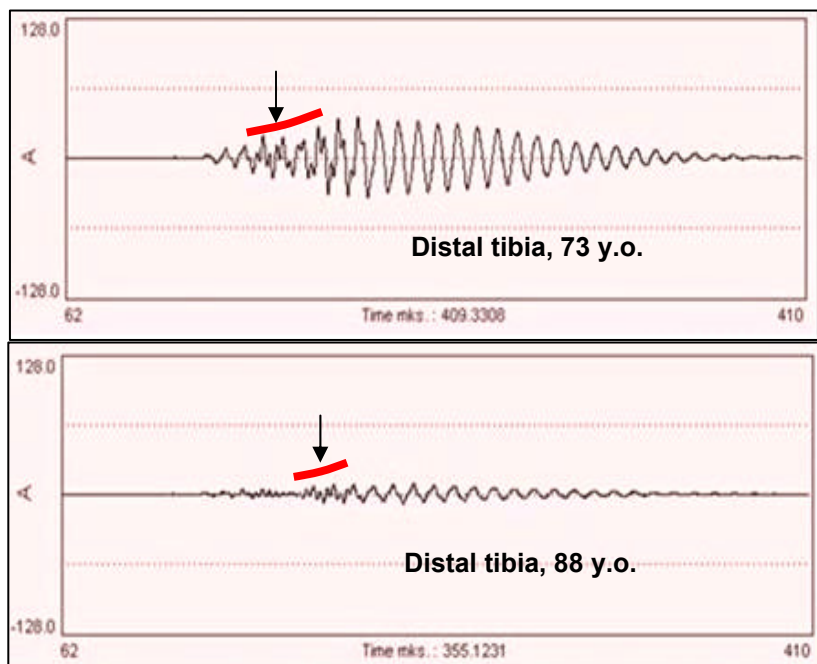

Figure 7.6. Surface transmission signals at 100 kHz in distal tibia of 73 and 88 year old donors. The signal in older bone is characterized by higher attenuation and slower propagation of surface wave front (marked by red arrow)

8. Coordination and Cooperation between Team Members and Industry Partners

The team worked successfully together during the reported period. The team members work in close contact with each other. The cooperation between the team members is excellent, as can be seen from the experimental part of this report as well as from the part related to the visualization and assessment of the data and building of the bone models with Rapid Prototyping. The international cooperation between German, Austrian, and Swiss partners have already led to results which could not have been obtained if this project had been based on national resources alone.

The coordination between the academic teams and the industrial partners Scanco Medical AG and Siemens AG has been excellent. Both industrial partners contribute very valuable resources and services to this project. Without the contributions from the industrial partners this project would not have been possible.

Scanco Medical AG has provided its know-how in regards of the most up-to-date µCT-scanner and the 3D-pQCT XtremeCT scanner. Academic partners CBF and MPICI are in telephone and email contact with Scanco (Bruno Koller and colleagues). Patients' data from distal tibia were acquired with XtremeCT 3D-pQCT scanner. In addition, the entire vertebral bodies were scanned by Scanco and high-quality 3D µCT-data sets were received by the team during the Phase II of the project. These data are crucial and are used by all academic partners. The µCT and 3D-pQCT systems developed by Scanco are unique as it is currently the only system that makes this possible.

Computed Tomography Division of Siemens AG, Siemens Medical Solutions (Thomas von der Haar and Christian Asbeck) organized technical support of the experiments and data acquisition on CT-scanners available at CBF. The representatives from Siemens made valuable comments and suggestions to the research activities. In addition, the information and recommendations provided by Siemens's was very valuable to us in the interpretation of the results of our CT experiments we made in Phase II of the Project and led to an optimization of the acquisition parameters for imaging of bone specimens during the present Phase III of the Project.

9. Publications and Contributions to Scientific Meetings

(After the time of the Final Report, Phase II)

Publications:

1. N. Marwan, A. Groth, J. Kurths. Quantification of Order Patterns Recurrence Plots of Event Related Potentials, *Chaos and Complexity Letters*, **2** (2/3), 301–314, 2007.

2. N. Marwan, J. Kurths, P. Saparin. Generalized Recurrence Plot Analysis for Spatial Data, *Physics Letters A*, **360** (4–5), 545–551, 2007.

3. N. Marwan, M.C. Romano, M. Thiel, J. Kurths. Recurrence Plots for the Analysis of Complex Systems, *Physics Reports*, **438** (5–6), 237–329, 2007.

4. N. Marwan, P. Saparin, J. Kurths. Measures of complexity for 3D image analysis of trabecular bone, *The European Physical Journal – Special Topics*, **143** (1), 109–116, 2007.

5. S. Prohaska. Skeleton-Based Visualization of Massive Voxel Objects with Network-Like Architecture. PhD thesis, University of Potsdam, July 2007.

6. P. Saparin, J.S. Thomsen, J. Kurths, G. Beller, W. Gowin. Segmentation of bone CT images and assessment of bone structure using measures of complexity, *Medical Physics*, **33** (10), 3857–3873, 2006.

Contributions to Scientific Meetings:

1. N. Marwan. Recurrence Plot basierte Biosignalverarbeitung. DGBMT-Workshop Biosignalverarbeitung, Potsdam, Germany, July 13-14, 2006.

2. N. Marwan, M.C. Romano, M. Thiel, J. Kurths. Recurrence Plots for the Analysis of Complex Systems. 2nd International Recurrence Plot Workshop, Siena, Italy, September 10-12, 2007.

3. A. Tatarinov, P. Saparin. Ultrasonic assessment of trabecular structure in proximal tibia. 2nd European Symposium on Ultrasonic Characterization of Bone, Halle, Germany, July 19-20, 2007.

10. Brief Review of Activities for the Second Part of the Project

These activities will be executed accordingly to the Statement of Strategic Objectives and the Task List stated in the CCN003. In details, the following activities are planned:

1. MRI imaging of bone specimens harvested during the first part of this Project. Acquisition of 3D MRI imaging from 10 patients with confirmed osteoporosis and 10 healthy volunteers.

2. Further building and mechanical testing of RP-models of test 3D cellular structures and RP-models of trabecular bone at different stage of osteoporosis based on µCT-data.

3. Comparison of fracture mechanisms in plastic models of regular structures and trabecular bone.

4. Study of relation between bone architecture and bone strength at different stages of osteoporosis. Comparison of bone strength in different loading directions using RP models.

5. Possibility to use existing device developed at MPIKG for mechanical loading of resin models and bone samples during µCT examination will be assessed.

6. Processing of more patients' 3D-pQCT data from ADOQ study and evaluation of trabecular bone structure by the developed measures.

7. Experiments to test stability and estimate reproducibility of the results bone of structural evaluation.

8. Analysis of spatial variation of the measures and relation between the structural measures and architecture.

9. Development of new types of measures based primarily on mechanical considerations will include:
   − Quantification of a link between the mechanical "weakness" of a node (joint) and the strain energy pattern induced when it is inserted as a defect in a regular lattice.
   − Application of the node analysis model developed for hexagonal geometries to architectures more closely related to that of trabecular bone, i.e. nodes with a coordination number of four leading to more rectangular geometries, and to extend the approach to three dimensions.
   − Extension of the model describing deformation localisation to non-Bravais lattices and to three dimensions in order to better approximate the actual structure of trabecular bone.
   − Extension of the lattice dynamics model to systems containing defects.

10. Application of the bone remodelling simulation to investigate the question whether bone cells need to communicate directly in order to produce and maintain trabecular bone, or whether this can be achieved indirectly through the coupling with mechanics and architecture

11. Implementation of the time dependence phenomenon of mineralisation into the bone remodelling model which results in a heterogeneous distribution of mineral content and hence elastic moduli throughout the bone structure.

12. Development of a method to track architectural elements through series of data sets and visualize architectural changes detected. This includes:
   − Elements will be tracked through complete data series based on volume overlap.

- Knowledge about the adjacency of elements will be exploited to improve the stability in case of unclear correspondence of elements.

- Events, like splitting and merging, will be detected.

- The information acquired from tracking elements will be displayed to the user.

- The procedure will be evaluated on several data series.

13. Visualization of relations between structural measure and architecture: structural measures will be associated with elements and visualized to reveal relations between measure and architecture.

14. Development of processing software for ultrasonic signals in surface transmission and reflection modes aimed to determine quantitative measures to be correlated with bone structure and comprising steps of statistical averaging, noise filtering, frequency filtering, 2D presentation and parameters calculation;

15. Ultrasonic testing of synthetic phantoms mimicking changes of structural parameters of the trabecular bone and analysis of analogies with ultrasonic data in real bones.

16. Correlation of ultrasonic parameters with available parameters of bone structure based on bone density and 3D morphometry, provided by partners. Conclusions on applicability of ultrasonic parameters for assessment of bone condition through correlations with changes of trabecular structure

11. References

Bertsch, A., Lorenz, H., Renaud, P. (1999) 3D micro fabrication by combining microstereolithography and thick resist UV lithography, *Sensors and Actuators*, **73** (1), 14–23.

Born, M. and K. Huang (1954). Dynamical Theory of Crystal Lattices. Oxford, Oxford University Press.

Boutroy, S., Bouxsein, M.L., Munoz, F., Delmas, P.D. (2005) In Vivo Assessment of Trabecular Bone Microarchitecture by High-Resolution Peripheral Quantitative Computed Tomography, *The Journal of Clinical Endocrinology & Metabolism*, **90** (12), 6508–6515.

Envisiontec GmbH (2006), Envisiontec Rapid Prototyping System: Perfactory Hardware Documentation, Perfactory Software Documentation, Edition 2006, Envisiontec GmbH, Gladbeck, Germany. See also www.envisiontec.de.

Envisiontec GmbH (2007), Envisiontec Perfactory R5 – R11 Material Documentation, Edition 2007, Envisiontec GmbH, Gladbeck, Germany.

Final Report Phase I (2003), 2D and 3D Quantification of Bone Structure and its Changes in Microgravity Condition by Measures of Complexity, Project ESA AO-99-030, ESTEC contract #14592/00/NL/SH.

Final Report Phase II (2006), 2D and 3D Quantification of Bone Structure and its Changes in Microgravity Condition by Measures of Complexity, Project ESA AO-99-030, ESTEC contract #14592/00/NL/SH, CCN001, CCN002.

ImageMagick Studio LLC (1999-2007), http://www.imagemagick.org.

Khachaturyan, A. G. (1983). Theory of Structural Transformations in Solids. New York, John Wiley and Sons.

Lehmann, T.M., Gönner, C., Spitzer, K. (1999) Survey: Interpolation methods in medical image processing, *IEEE Trans. Med. Imaging*, **18** (11), 1049–1075.

Marwan, N., Saparin, P., Thomsen, J.S., Kurths, J. (2005). An Innovative Approach for the Assessment of 3D Structures in Trabecular Bone. *J Grav Physiol*, **12**, 127–128.

Marwan, N., Saparin, P., Kurths, J. (2007). Measures of complexity for 3D image analysis of trabecular bone, *The European Physical Journal – Special Topics*, **143**, 109–116.

Milos, G., Spindler, A., Rüegsegger, P., Seifert, B., Mühlebach, S., Uebelhart, D., Häuselmann, H. (2005) Cortical and trabecular bone density and structure in anorexia nervosa, *Osteoporos Int.*, **16** (7), 783-90.

Milos, G., Spindler, A., Rüegsegger, P., Hasler, G., Schnyder, U., Laib, A., Gallo, L.M., Uebelhart, D., Häuselmann, H. (2007) Does weight gain induce cortical and trabecular bone regain in anorexia nervosa? A two-year prospective study. *Bone* [Epub ahead of print, August 7, 2007].

Nazarian, A. and R. Müller (2004). Time-lapsed microstructural imaging of bone failure behavior *Journal of Biomechanics* **37**, 55-65.

Pistoia, W., van Rietbergen, B., Lochmüller, E.-M., Lill, C.A., Eckstein, F., Rüegsegger, P. (2004) Image-Based Micro-Finite-Element Modeling for Improved Distal Radius Strength Diagnosis. Moving From "Bench" to "Bedside". *Journal of Clinical Densitometry*, **7** (2), 153-160.

Prohaska, S. (2007). Skeleton-Based Visualization of Massive Voxel Objects with Network-Like Architecture. PhD thesis, University of Potsdam, July 2007.

Roerdink, J. & Meijster, A. (2000). The watershed transform: Definitions, algorithms and parallelization strategies. *Fundamenta Informaticae*, **41** (1-2), 187–228.

Saparin, P., Thomsen J.S., Prohaska, S., Kurths, J., Zaikin, A., Hege, H.-C., Gowin, W. (2005). Quantification of Spatial Structure of Human Proximal Tibial Bone Biopsies Using 3D Measures of Complexity, *Acta Astronautica,* **56**, 820–830.

Sheskin, D.J. (2004) Handbook of parametric and nonparametric statistical procedures, 3-rd ed., Boca Raton, Chapman & Hall / CRC.

Stauber, M. and R. Müller (2006). Age-related changes in trabecular bone microstructures: global and local morphometry *Osteoporosis International* **17**, 616-626.

Tatarinov, A., Gowin, W., Beller, G., Saparin, P. (2005) A perspective for ultrasonic assessment of osteoporotic changes of bone structure in proximal tibia. *J. Grav. Physiol.*, **12** (1): 139-140.

Woesz, A., Stampfl, J., Fratzl, P. (2004) Cellular solids beyond the apparent density - an experimental assessment of mechanical properties, *Adv. Eng. Mat.*, **6** (3), 134–138.

Yanson, H.A., Tatarinov, A.M., Dzenis, V.V., Kregers, A.F. (1984) Constructional peculiarities of the human tibia defined by reference to ultrasound measurement data, *Biomaterials*, **5** (4), 221–226.